Ore Geology Reviews 105 (2019) 86–101

Contents lists available at ScienceDirect

Ore Geology Reviews

journal homepage: www.elsevier.com/locate/oregeorev

Defining IOCG signatures through compositional data analysis: A case study of lithogeochemical zoning from the Olympic Dam deposit, South Australia

Marija Dmitrijeva[a,*], Kathy J. Ehrig[b], Cristiana L. Ciobanu[a], Nigel J. Cook[a], Max R. Verdugo-Ihl[a], Andrew V. Metcalfe[c]

[a] School of Chemical Engineering, The University of Adelaide, Adelaide, SA 5005, Australia
[b] BHP Olympic Dam, Adelaide, SA 5001, Australia
[c] School of Mathematical Sciences, The University of Adelaide, Adelaide, SA 5005, Australia

ARTICLE INFO

Keywords:
Principal component analysis
Hierarchical clustering
Whole-rock dataset
IOCG deposits
Lithogeochemical zoning
Olympic Dam

ABSTRACT

The Olympic Dam Cu-U-Au-Ag deposit is dominantly composed of mineralised hematite-breccias and occurs entirely within the Roxby Downs Granite. Multivariate statistical analysis of a large whole-rock, 15 m-interval geochemical dataset (10,565 samples) was undertaken to identify geochemical signatures characteristic of iron-oxide copper gold (IOCG)-style mineralization and constrain the conspicuous lithogeochemical zonation observed at Olympic Dam. Statistical analyses include principal component analysis on centred logratio (clr)-transformed data coupled with hierarchical clustering. Certain groups of elements that can be interpreted in terms of an evolving hydrothermal system relative to host lithologies are derived from data analysis: granitophile (U-W-Sn-Mo); siderophile (Ni-Co); chalcophile (Ag-Bi) and related elements (As-Sb and Au-Te). The distributions of elements within each group are investigated through three vertical cross-sections and are compared with known lithological and Cu-(Fe)-sulphide zonation. Throughout the Olympic Dam Breccia Complex, the IOCG signature is defined by multi-element combinations of the commodity metals Cu, U, Au, and Ag, coupled with a range of trace elements. Overall, the IOCG signature overlaps well with Fe-metasomatism despite mismatch which is likely due to discrete styles of mineralisation found only on the margins of the deposit and also to the presence of mineralised domains within Fe-poor zones. The IOCG signature is composed of two geochemical associations, which exhibit distinct spatial distributions. The first group, Cu-U_3O_8-Se-S, shows concentric zonation whereas the second group, Au-W-Mo-Sb-As, forms a vertical ~1800 m deep corridor in the southeastern lobe of the deposit. The specific Au-W-Mo-As-Sb signature could potentially be generic within IOCG systems across the Olympic Cu-Au province and if so, would provide a proxy model for near-mine exploration.

1. Introduction

A distinctive feature of many magmatic-hydrothermal ore deposits is the presence of systematic spatial distribution patterns, commonly expressed by zoned alteration assemblages and/or paragenetic sequences (e.g., Guilbert and Park, 1986). The spatial distribution of minerals, and hence the suite of elements that each contains, occurs due to fluid flow in and around intrusive bodies and conduits for hydrothermal fluids as a response to pH, Eh, temperature gradients and other factors. Investigation of the spatial distribution of mineral assemblages and mineral compositions in deposits formed by dynamic fluid/rock reactions as, for example, in skarn deposits (e.g., Meinert, 1997) is crucial for the development and validation of hypotheses concerning ore genesis that can underpin conceptual exploration models.

Magmatic-hydrothermal iron-oxide copper gold (IOCG) deposits (e.g. in Olympic Cu-Au Province, South Australia; the Cloncurry District, Queensland, or the Carajás Mineral Province, Brazil) represent an economically significant source of Cu, Au, Ag, and in some cases, also U. These deposits are also enriched in, and thus represent potential resources for rare earth elements (REE), and several minor elements, including Co, Nb, and Te (Barton, 2014). The IOCG clan encompasses a diverse group of deposits found in a range of geological settings, and formed from the Archean to Tertiary (e.g., Groves et al., 2010). Despite such a broad spectrum of IOCG systems in terms of age, regional setting, genetic characteristics, host rocks, and ore grade, they are all inherently associated with zoned alteration envelopes and contain significant, often dominant concentrations of Fe-oxides (Barton, 2014, and references therein). In conceptual models for IOCG systems, the expression of regional-scale hydrothermal alteration varies from distal alkali-rich to proximal hydrolytic sericite-chlorite assemblages (Hitzman et al.,

* Corresponding author.

https://doi.org/10.1016/j.oregeorev.2018.12.013
Received 8 October 2018; Received in revised form 8 December 2018; Accepted 17 December 2018
Available online 18 December 2018
0169-1368/

1992). Zonation patterns can be tracked at different scales, from alkali-rich metasomatism observable on the district-scale (e.g., Cloncurry, Queensland, Australia; Oliver et al., 2004; the Moonta area in the Gawler Craton, South Australia; Conor et al., 2010; Kontonikas-Charos et al., 2014), down to within individual deposits (e.g., Ernest Henry, Queensland; Mark et al., 2006). Such zonation patterns may also be expressed by changing compositions or concentrations of trace elements within minerals approaching the orebody (e.g., Ismail et al., 2014).

The Olympic Cu-Au Province, South Australia, is one of the best-endowed Proterozoic IOCG provinces on Earth and comprises deposits/prospects associated with a major tectono-magmatic event at ~1.6 Ga (Skirrow et al., 2007). Olympic Dam (OD) is by far the largest single deposit in the province and exhibits remarkable lateral and vertical mineralogical zonation with respect to Cu-(Fe)-sulphides among others (Ehrig et al., 2012). Sulphide distribution patterns are defined by an inwards transition from pyrite-chalcopyrite (Py-Cp), chalcopyrite-bornite (Cp-Bn) and bornite-chalcocite (Bn-Cc), observable also vertically from deeper to shallower levels. The deposit is well-suited for understanding geochemical patterns versus mineral zoning because of the relatively simple geological setting. The orebody is hosted within a breccia complex with various degrees of Fe-metasomatism, all enclosed within a host granite (e.g., Ehrig et al., 2012).

In this contribution, we address lithogeochemical zoning in the OD deposit with principal component analysis (PCA) and hierarchical clustering, using a large (10,565-sample) whole-rock geochemical dataset encompassing 39 elements. These exploratory multivariate statistical methods are required for making data-driven decisions on grouping variables, i.e., elements that define the specific geochemical signatures of IOCG systems, and to circumvent the large dimensionality of multi-element data. The combination of multivariate statistical methods and large whole-rock geochemical data offers potential insights that can constrain genetic models, identify potential sources of metals and fluids, and assert the nature, relative timing and mechanisms of superimposed overprinting events. Outcomes have application to other ore systems in comparable settings.

2. Geological background and rationale

The OD deposit is associated with rocks of the bimodal Gawler Silicic Large Igneous Province (SLIP) in the eastern Gawler Craton (Allen et al., 2008). The Gawler SLIP comprises intrusive rocks of the Hiltaba Suite (HS), and cogenetic extrusive equivalents assigned to the Gawler Range Volcanics (GRV). Within the OD deposit, the latter include intensively altered olivine-phyric and dolerite dykes (Huang et al., 2015; 2016) and breccias dominated by felsic volcanic fragments (Ehrig et al., 2012). Fresh dolerite dikes attributed to younger, 820 Ma Gairdner Large Igneous Province are also present (Huang et al., 2015). The deposit is entirely contained within the Olympic Dam Breccia Complex (ODBC) which is predominantly derived from the host Roxby Downs Granite (RDG) (Reeve et al., 1990). The southeastern areas of the ODBC contain the greatest density of sedimentary facies rocks at shallow depths immediately below the unconformity (McPhie et al., 2016). The deposit lies immediately below a major unconformity and is overlain by sedimentary rocks of the Stuart Shelf.

The ODBC comprises varied assemblages containing ore and gangue minerals of hydrothermal origin, as well as relict minerals derived from altered lithologies. The most widespread minerals (in order of abundance) are hematite, quartz, sericite, orthoclase, chlorite, siderite, fluorite, baryte, pyrite, chalcopyrite, bornite and chalcocite (Ehrig et al., 2012). Mineralogical studies of magmatic feldspars and accessory apatite from igneous rocks and hydrothermal minerals from the orebody (uraninite, hematite, REE-fluorocarbonates and Cu-(Fe)-sulphides) show preservation of primary characteristics despite being affected by superimposed fluid-rock interaction (Macmillan et al., 2016a,b,c; Krneta et al., 2016; Ciobanu et al., 2017; Kontonikas-Charos et al., 2017; Schmandt et al., 2017; Verdugo-Ihl et al., 2017). These studies show widespread evidence for rock-buffered reactions (replacement via coupling dissolution with reprecipitation rates; Putnis, 2002), inferring that reworking of mineral assemblages can take place on the scale of microns to meters if the porosity is not sustainably networked. This allows the hydrothermal alteration assemblages to preserve the gradational continuum observed within the ODBC. The continuum ranges from sericite-hematite alteration, becoming more pervasive and intense from peripheral, weakly-altered non-mineralized RDG to hematite-dominant breccias within the deposit centre (Ehrig et al., 2012; Mauger et al., 2016; Kontonikas-Charos et al., 2017).

Economic concentrations of Cu-(Fe)-sulphides are predominantly contained within hematite-rich breccias and a strong association between Fe-metasomatism and Cu-mineralization is thus expected (Fig. 1a). The concentric zonation of Cu-(Fe)-sulphides is enveloped around an L-shaped, Cu-barren, high-Fe, quartz-baryte-bearing

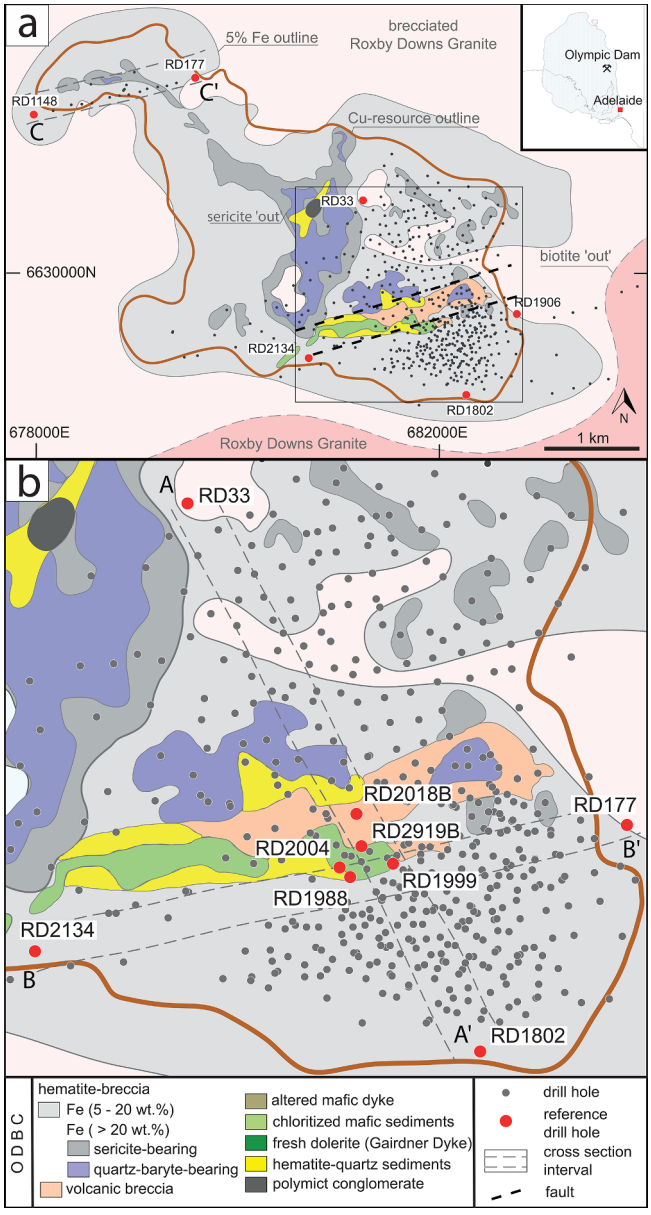

Fig. 1. Simplified geological map (coordinate system WGS 1984 UTM Zone 53S; after Ehrig et al., 2012) indicating the outline of the Olympic Dam Breccia Complex, drillhole collar locations, and cross-section CC' in the northwestern arm (a); the location of the cross-sections AA' and BB' in the southeastern lobe (b). The map is representative of geology projected at 350 m below the surface.

hematite breccia that is mainly restricted to the central part of the ODBC (Fig. 1a; Reeve et al., 1990; Ehrig et al., 2012). These Cu-barren breccias were originally interpreted as hydrothermal fluid centres and maar-diatreme structures that represent nested eruption/collapse craters that subsequently incorporated and accommodated blocks of RDG, GRV, and assorted epiclastic and sedimentary facies (Reeve et al., 1990). The proposed model accounting for deposit zonation enveloping a central, highly-altered, low-sulphide zone (Fig. 5 in Reeve et al., 1990), became untenable following interpretation of closely-spaced drilling which intersected discovery of ~2 km-thick mineralised interval in the southeastern lobe of the deposit (Ehrig et al., 2012, 2017, and references therein). Further asymmetry is shown by presence of mineralization at a depth below ~1.5 km (and still open at 2.3 km) within felsic volcanic rocks on the SE margin of the deposit (Apukhtina et al., 2017). A shallow, maar-diatreme model would also require a subvolcanic environment, which although not completely ruled out by the RDG emplacement depth of 6–8 km [from petrographic studies of Creaser (1989) and feldspar-amphibole geothermobarometric estimates of Kontonikas-Charos et al. (2017)], does not explain why mineralization is hosted by altered granite. In addition, the central part of the deposit, considered in earlier studies as a fluid conduit (Reeve et al., 1990), is interpreted in the latest model as a result of vertical faults with multiple episodes of activation post-dating the lifespan of the ~1.6 Ga IOCG event (Cherry et al., 2018).

Therefore, deep mineralization intersected by drillhole RD1988 (Fig. 1b; Ehrig et al., 2012) suggests the presence of fluid centres deeper than previously recognised. Moreover, the RDG setting opens-up the idea that mineralisation could have been initiated at depth, from multiple fluid sources released from the granite cupola prior to its uplift. In magmatic-hydrothermal systems, vertical and lateral zonation with respect to mineral assemblages mirrors the spatial distribution of mineralization relative to the fluid source. Although it is difficult to reconcile both the concentric Cu-(Fe)-sulphide zonation with the occurrence of deep mineralization at the southeastern edge of the ODBC to a single simultaneous point of fluid entry, the present deposit zonation is most likely the result of both primary and superimposed effects. Faults (and their reactivation) and/or erosion of the upper parts of the deposit are considered particularly significant.

Altogether, the pronounced deposit zonation, coupled with an apparently simple granite-hosted setting, make OD an ideal target to test if there are other geochemical patterns that can be related to the Cu(-Fe)-sulphide zoning and if these display concentration gradients relative to potential fluid pathways. As a first step towards constraining geochemical gradients within the ODBC, we address the zonation patterns of metals with emphasis on lithological classes and Cu(-Fe)-sulphide mineral zonation patterns. The study aims to test whether certain trace elements, grouped according to multivariate statistical analyses, match the observed mineralogical and alteration zonation. Specifically, this work addresses the characteristic association of a distinct suite of 'granitophile' elements (U, W, Sn and Mo) identified at OD, and defining the distinct geochemical identity of the abundant primary oscillatory-zoned hematite (Ciobanu et al., 2013; Verdugo-Ihl et al., 2017). Understanding geochemical gradients not only allows inference of the hydrothermal evolution of the deposit, but also offers ways to distinguish between primary metallogenic patterns and trace element signatures attributable to superimposed processes.

3. Methods and data

3.1. Sample suite

The whole-rock multi-element geochemical dataset used for this study consists of 10,565 samples from 540 separate drillholes. Assay data were collected regularly from 15 m-long intervals along the drillcores and form a dense grid in the southeastern lobe of ODBC, and a transect in the northwestern arm of the deposit (Fig. 1a, b). A small number of drillholes which were sampled at 1, 2, 2.5 and 5 m-long intervals were recalculated to 15 m intervals. This study does not consider the northern domain of the ODBC due to the limited availability of whole-rock data. However, a single section across the extreme northwestern part of the ODBC is included.

All drill core samples were assayed for the same suite of elements by Bureau Veritas (Adelaide). Four-acid digestion (HCl-HNO_3-HF-$HClO_4$) and metaborate/tetraborate fusion were used to ensure total dissolution of all minerals. As given by Ehrig et al. (2012), analysis was achieved by four-acid digestion and inductively coupled plasma-optical emission spectroscopy (IP-OES) for Cu, Ag, As, Co, Ni, Pb, and Zn; lithium metaborate/tetraborate fusion and ICP-OES for Ba, Al, Ca, Ce, Fe, K, La, Mg, Mn, Na, P, Si, Sr, Ti, Y, and Zr; lithium metaborate/tetraborate fusion and inductively coupled plasma-mass spectroscopy for U_3O_8, Bi, Sb, and Mo; induction furnace-infrared spectrometry for CO_2 and S; and fire assay-flame atomic absorption spectrometry for Au. Essentially the same dataset is reported by Ehrig et al. (2012) and underpins the deposit-scale zonation patterns described therein. Summary statistics are provided in an appendix to Ehrig et al. (2012).

The sample suite covers the majority of lithologies present in the ODBC. A simplified classification for various hematite- and granite-breccias is based on the proportion of Fe wt. % and the presence/absence of aluminosilicates, mainly sericite (Table 1). Such an approach is appropriate to characterize the body of mineralized rocks within the ODBC.

The largest domain of sedimentary and volcanic rocks in the dataset (~2% and ~7% of the data, respectively) are present in the southeastern lobe of the ODBC (Fig. 1b). These lithologies form a WSW-ENE-trending lineament (Fig. 1) with vertical plunge down to depths of ~1 km. Quartz-baryte-bearing hematite breccias (~5% of data) are also dispersed in proximity to the volcanic and sedimentary rocks along the WSW-ENE lineament and are best developed in the middle part of the deposit (Fig. 1b). The sample suite also includes data for mafic dikes, which can be sub-divided into: (i) strongly altered rocks considered as mafic/ultramafic rocks coeval with 1.59 Ga magmatism; and (ii) fresher basaltic/dolerite rocks considered affiliated to the ~ 820 Ma Gairdner Dyke Swarm (Huang et al., 2015). Such mafic dikes, although intersected in 43 drillholes, are very minor constituent in the present dataset (< 2% of the data).

Geochemical signatures within the ODBC are investigated through three deposit-scale cross-sections, each covering drillholes within a 200 m-wide band (Fig. 1): a ~NW-SE cross-section crosscutting the southeastern part of the deposit (section AA'); a ~W-E profile placed along the strike of the domain of sedimentary and volcanic breccias in the SE lobe (section BB'); and a ~W-E profile along the length of the NW arm of the deposit (section CC').

3.2. Data processing

Left-censored values are measurements that fall below the minimum detection limit (mdl) and may thus introduce considerable inconsistence into the data (Helsel, 2006). In geochemical data analysis it is common to replace mdl values with a fraction of that value, for instance one half of mdl, however, this approach is to be avoided as it changes the relative variation structure in compositions (Palarea-Albaladejo and Martín-Fernández, 2013, 2015).

Within the OD dataset, the proportion of values below mdl varied depending on the measured element: it exceeded 50% for Cr, Ta, Tm, and V, and was close to 30% for Mn and Se. For all remaining elements, left-censored values were imputed using robust multiplicative log-normal replacement, a routine available from the 'zCompositions' package in R (Palarea-Albaladejo and Martín-Fernández, 2015). This method respects the geometry of the compositional data and preserves the ratios among D-part components in a composition, being thus a reasonable choice for an imputation technique.

Table 1
Simplified description of the main lithologies of the ODBC with corresponding nomenclature from literature; percentage of whole-rock data attributed to each lithological class is reported.

Lithology	Description	Percentage	Corresponding nomenclature and comments
Brecciated Roxby Downs Granite	Brecciated and altered granite with hematite as a matrix component of a clast-supported breccia	0.5	
Hematite breccia Fe (5–20 wt% Fe)	Hematite breccia with altered and progressively obliterated Roxby Downs Granite fragments; hematite is present as a matrix component, occasionally as pseudomorphic replacements after inherited granitic components	54	
Sericite-bearing hematite breccia Fe (> 20 wt%)	Hematite breccia with hematitic infill and almost fully hematitized and/or sericitised Roxby Downs Granite fragments; displays a more intense alteration and a strong association with sulphides	30	
Quartz-baryte-bearing hematite breccia (> 20 wt% Fe)	Hematite breccia with fragments of hematite and quartz which are placed within hematitic infill; Cu- and U-barren, the breccia lacks sulphides and aluminosilicates, although it comprises significant Au mineralization	5	As HEMQ in Ehrig et al. (2012)
Volcanic breccia	Hematite-rich breccia with intensely altered and reworked felsic and/or mafic-ultramafic clasts	7	The incorporated clasts are interpreted as relicts of felsic and mafic lavas of Gawler Range Volcanics (Ehrig et al., 2012)
Altered mafic-ultramafic dyke	Sericitised and/or chloritized, aphanitic, doleritic and porphyritic mafic dykes	1	~1590 Ma olivine-phyric basalts and dykes (Huang et al., 2016)
Fresh dolerite (Gairdner Dyke)	Green, Ti-magnetite-bearing dolerite dykes	0.5	Gairdner basaltic to doleritic dykes (Huang et al., 2015)
Chloritized mafic sediments	Laminated, chlorite-bearing sedimentary rock	1	As green sandstone and mudstone (McPhie et al., 2016); or KASH (Ehrig et al., 2012)
Hematite-quartz sediments	Laminated, hematite-rich sedimentary rock	1	As interbedded sandstone and red mudstone (McPhie et al., 2016) or KHEMQ (Ehrig et al., 2012)

3.3. Multivariate statistical analyses

3.3.1. Hierarchical clustering

Hierarchical cluster analysis of a 39-part sub-composition containing major and trace elements, Ag, Al, Au, As, Ba, Bi, Ce, Cl, Co, CO_2, Cu, F, Fe, Ga, K, Mg, Mn, Mo, Na, Nb, Nd, Ni, P, S, Sb, Se, Sb, Si, Sn, Sr, Ta, Te, Th, Ti, U_3O_8, W, Y, Zn, and Zr, was performed to explore the geochemical affinities among elements. In this study, correlation and covariance matrix of untransformed raw data were avoided due to the spurious effects of compositional data closure (Pearson, 1897; Aitchison, 1986). Instead, clustering was based on the variation matrix (Appendix A; Table 2). The entries of the matrix are the variances of the logratios of the elements (Aitchison, 1986)

$$\tau_{ij} = var(\ln(x_i/x_j)) \quad (1)$$

for i, j from 1 to 39. A small τ_{ij} indicates a small variance of $\ln(x_i/x_j)$, thus implying a degree of proportionality between elements x_i and x_j. In the variation matrix, perfect proportionality between two components is represented as zero. The variation matrix is preferred to the correlation matrix as a distance measure among the components of compositions (van den Boogaart and Tolosana-Delgado, 2013). Conversion of variation matrix into a distance matrix was done using Euclidean metric space, and it was followed by the complete linkage agglomeration method, which implies sequential merging of similar clusters as dictated by the distance measure.

Table 2
Variation matrix (Eq. (1)). The extended version of the variation matrix is in Appendix A.

Variable	Ag	Au	As	Ba	Bi	Ce	Co	Cu	Ga	Mo	Nb	Nd	Ni	S	Se	Sb	Sn	Ta	Te	Th	U_3O_8	W	Y	Zr
Au	1.9																							
As	2.0	1.7																						
Ba	3.1	3.0	1.4																					
Bi	1.0	1.8	1.5	2.5																				
Ce	1.0	1.2	1.2	2.0	0.9																			
Co	1.9	3.0	3.1	4.7	2.0	1.5																		
Cu	1.7	2.7	3.8	4.9	1.9	1.9	2.1																	
Ga	1.4	2.5	1.9	2.5	1.7	0.9	1.3	2.9																
Mo	1.5	1.3	0.9	1.7	1.2	0.8	2.5	2.5	1.7															
Nb	1.3	2.1	1.8	3.1	1.6	0.9	1.3	2.8	0.7	1.8														
Nd	0.9	1.5	1.3	2.2	0.9	**0.1**	1.3	1.9	0.7	1.0	0.7													
Ni	2.2	3.4	2.9	4.5	2.4	1.9	0.9	3.1	1.3	2.8	1.3	1.6												
S	1.5	1.8	2.1	3.0	1.4	1.0	1.4	1.4	2.0	1.2	1.6	1.1	2.1											
Se	2.0	2.7	3.0	4.8	2.3	1.9	1.9	2.4	2.3	2.8	1.6	1.8	2.2	1.9										
Sb	2.0	1.9	**0.4**	1.3	1.5	1.2	3.2	3.7	1.8	0.9	2.0	1.4	3.0	2.1	3.3									
Sn	1.4	1.8	1.1	2.2	1.4	0.8	2.1	3.1	1.1	1.1	0.9	0.7	2.2	1.6	2.4	1.2								
Ta	1.6	2.8	2.1	2.9	2.0	1.2	1.4	3.2	**0.3**	2.0	0.7	1.0	1.4	2.1	2.3	2.2	1.4							
Te	1.3	1.5	1.1	2.0	1.3	0.7	2.3	2.7	1.4	0.8	1.3	0.7	2.4	1.4	2.6	1.1	0.8	1.7						
Th	1.8	3.2	2.6	3.1	2.2	1.3	1.6	3.3	**0.2**	2.3	1.0	1.1	1.6	2.5	2.7	2.5	1.6	**0.4**	1.9					
U_3O_8	1.0	1.7	2.2	3.4	1.1	**0.6**	1.1	1.0	1.4	1.4	1.1	**0.6**	1.8	0.8	1.6	2.2	1.5	1.6	1.4	1.7				
W	1.5	1.2	0.8	1.8	1.3	0.8	2.6	2.8	1.9	**0.6**	1.7	1.0	2.9	1.3	2.6	0.8	0.9	2.2	0.8	2.6	1.5			
Y	1.1	2.3	1.9	2.7	1.3	**0.6**	1.0	2.2	**0.3**	1.6	**0.6**	**0.4**	1.2	1.4	1.9	1.8	1.0	**0.6**	1.2	**0.6**	0.8	1.6		
Zr	2.3	3.7	2.8	3.0	2.7	1.8	2.2	4.0	**0.4**	2.6	1.6	1.7	2.0	3.1	3.4	2.7	2.0	**0.6**	2.3	**0.3**	2.4	3.0	1.0	
Zn	2.1	3.5	2.5	3.3	2.4	1.7	1.8	3.6	1.0	2.5	1.6	1.5	1.7	2.7	3.1	2.5	1.9	1.1	2.1	1.1	2.1	2.7	1.2	1.2

*Numbers in bold indicate the strongest element pair codependence (≤ 0.6).

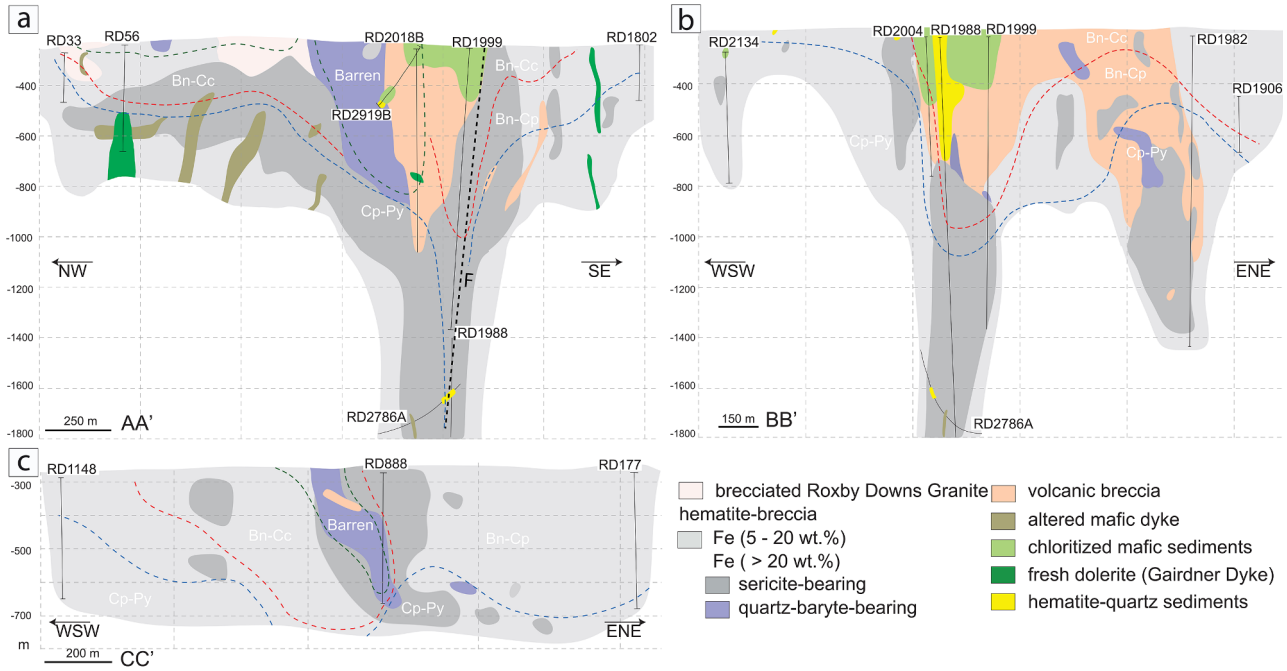

Fig. 2. Interpreted geological cross-sections featuring the distribution of lithological units in AA' (a), BB' (b) and CC' (c) with overlay of estimated Cu(-Fe)-sulphide zone boundaries (see Section 3.5). The cross-sections were reconstructed using core logging and the lithogeochemistry discussed in this study. The upper boundary of cross-sections represents the unconformity surface.

3.3.2. Principal component analysis

Principal Component Analysis (PCA) is frequently used for exploratory data analysis of multivariate data from geochemical studies to identify associations among elements that can be used to explain geological and geochemical processes (e.g. Grunsky, 2010; Grunsky et al., 2014; Chen et al., 2017). The method aims to find the maximum variation within the data by reducing its dimensionality and results in a linear combination of chemical elements defined as principal components (PCs). The outcomes of PCA are commonly presented as a biplot of scores (score of every sample on PC1 and PC2) and loadings (loadings of every element on PC1 and PC2) (Gabriel, 1971), whereas the positioning of loadings (i.e., elements), reflects geochemical affinities among the variables.

In this study, PCA was performed by singular values decomposition of centred logratio (clr) transformed data. The transformation is required to respect its simplicial geometry (Aitchison, 1986). The multivariate data analysis and corresponding calculations were performed in the R package 'compositions' (van den Boogaart et al., 2014).

3.4. Spatial 3D-modelling

Spatial modelling of continuous variables (i.e., element concentrations) was performed using the implicit 3D-modelling tool in Leapfrog Geo 3D software. The spatial models were derived by spheroidal interpolant function, i.e., semi-variogram, with a base range of 200 m and a constant drift. The cross-sections corresponding to lithological sections AA', BB' and CC' (Fig. 1) were derived as transects through the kriged surfaces of the SE-lobe and NW-arm. The location of cross-sections was chosen through the longest axis of densely populated drillholes (CC') and through the maximum lithological variability (BB').

3.5. Estimation of normative Cu-(Fe)-sulphide mineralogy

To approximate the deposit-scale sulphide-zonation, normative mineralogy calculations were used to estimate the proportion of sulphides based on whole-rock geochemical data, stoichiometric criteria and the predominant sulphide-assemblages. The employed approach considers the main S-bearing phases: baryte, pyrite, chalcopyrite, bornite and chalcocite; and native copper, following the following steps:

(1) Calculation of molar proportions for As, Ba, Cu, Ni, S, Sb and Zn;
(2) If the molar proportion of Ba ≥ S, then all S is converted to equivalent baryte and removed, otherwise equivalent amount of S in 1:1-ratio to Ba is removed;
(3) If S > 0 after step (2), then Sb and As are added to S (S*), whereas Ni and Zn are included with Cu (Cu*);
(4) The S*:Cu*-ratio is used to determine the sulphide-zone as following:
   a. If S*:Cu* > 2, then normative chalcopyrite is calculated (based on Cu*), which is then removed to subtract its equivalent from S* and then calculate normative pyrite with the remaining S* (→ 'Py-Cp-zone');
   b. Otherwise, if S*:Cu* > 0.8, then normative chalcopyrite is calculated by subtracting 0.8 from S*:Cu, dividing the difference by 1.2 and multiplying it by Cu*, after which the equivalent S* is removed, whereas normative bornite is then calculated by dividing the remaining S* by 4 (→ 'Cp-Bn-zone');
   c. Otherwise, if S*:Cu* > 0.5 (or < 0.8 if step 4d is not followed), then normative bornite is calculated by subtracting 0.5 from S*:Cu, dividing the difference by 0.3 and multiplying it by Cu* divided by 5, after which the equivalent S* is removed, whereas normative chalcocite corresponds to the remaining S* (→ 'Bn-Cc-zone');
   d. Otherwise, if (S*:Cu* ≤ 0.5), normative chalcocite corresponds to S*, which is removed from Cu*, after which the remaining Cu* corresponds to native copper. Since native copper is extremely sparse in the ODBC, the zone was amalgamated with 'Bn-Cc-zone';
   e. Regardless of the potential sulphide-zone, if Cu < 0.1 wt%, the zone is considered 'Barren'. The zones 'Py-Cp', 'Cp-Bn', 'Bn-Cc' and 'Barren' are used as categorical variables to project Cu(-Fe)-sulphide zonation onto cross-sections.

4. Results

The simplified geological cross-sections are given in Fig. 2a–c. All three cross-sections show interfaces between bornite-chalcocite ('Bn-Cc') and pyrite-chalcopyrite ('Py-Cp') zones and are thus representative of the complete ore zonation within the ODBC. In all cross-sections the 'Py-Cp' ore zone remains open at depth. The Cu(-Fe)-sulphide zonation (Fig. 2), which was calculated from the whole-rock data, broadly matches the patterns obtained from the MLA dataset reported by Ehrig et al. (2012).

CC' is a relatively shallow cross-section, down to a depth of only 800 m, and is based on a transect of just 15 equally-spaced drillholes in the NW arm (Fig. 2c). On the contrary, the southeastern cross-sections, AA' and BB', are deeper, intersect each other in drillhole RD1999 and are placed within the limits of the dense grid of drillholes (Fig. 1b). Cross-section BB' includes data from some of the deepest parts of the orebody, which remains open at a depth of ~1800 m (e.g., RD1988; Fig. 2b). The southeastern cross-sections feature greater lithological variability, containing sedimentary rocks and volcanic breccia as blocks ranging from shallow depths immediately below the unconformity to deeper parts of the ODBC (Fig. 2a, b). Although the interpretation of geological sections is reliable, based on the existing data, interpolation of continuous variables is inhibited due to the limited number of drillholes that continue below depths of ~1100 m in the southeastern lobe. The interpolant extents in the southeastern sections are therefore bounded at ~1100 m.

4.1. Hierarchical cluster analysis

The subset of the variation matrix displaying a 39-part sub-composition of the ODBC samples is shown in Table 2. The variation matrix reflects the degrees of proportionalities of elements and geochemical affinities among groups of elements. For instance, Ce shows the strongest co-dependency with Nd ($\tau_{CeNd} = 0.1$) followed by Ga and Th ($\tau_{GaTh} = 0.2$) and Sb and As ($\tau_{SbAs} = 0.4$). Tungsten shows a strong association with Mo ($\tau_{WMo} = 0.6$) and As ($\tau_{WAs} = 0.8$). In contrast, Ba shows the strongest disproportionality with Cu and Se ($\tau_{BaSe} = 4.8$; $\tau_{BaCu} = 4.9$). These associations are evident from the hierarchical clustering dendrogram (Fig. 3), which is based on the variation matrix (Appendix A; Table 2). The height of the dendrogram represents a measure of similarity among the elements and corresponds to a variation matrix. Therefore, merged groups of elements in the lower part indicate similarity.

Four distinct subgroups of elements can be distinguished. Group 1 encompasses K, Al, Zn, Zr, Ti, Si, Na, Th and Ga, along with Co and Ni, and represents the geochemical signatures of non-mineralized felsic and mafic intrusive rocks. In contrast, Groups 2, 3 and 4 are all elements characteristic of IOCG-style mineralization. Group 2 displays the association of Cu and U mineralization, also including Se. Group 3 specifically reflects a magmatic-hydrothermal granitic signature (Mo, W, and Sn, along with As, Sb, Au, and Te), whereby Au displays the

Table 3
Results from compositional principal component analysis. Bold numbers indicate elements with the largest loadings on principal components (> 0.19).

Eigenvalues of PC1 to PC3			
Eigenvalues	PC1	PC2	PC3
λ	3.55	2.56	1.95
λ%	32	15	9
$\sum\lambda$%	32	48	57
Loadings of the elements on PC1-PC3			
Elements	PC1	PC2	PC3
Ag	−0.09	−0.06	0.13
Al	**0.26**	0.11	0.09
Au	**−0.25**	0.01	0.08
As	**−0.20**	**0.21**	−0.09
Ba	−0.16	**0.36**	**−0.29**
Bi	−0.15	−0.03	0.01
Ca	−0.07	−0.10	−0.17
Ce	−0.11	0.00	0.01
Cl	0.10	0.03	0.08
Co	0.05	**−0.27**	0.09
CO_2	0.17	**−0.35**	**−0.58**
Cu	−0.13	**−0.29**	0.17
F	−0.01	−0.01	−0.10
Fe	−0.11	−0.05	0.01
Ga	0.10	0.09	0.05
K	**0.33**	0.16	0.03
Mg	0.19	−0.01	0.08
Mn	**0.24**	**−0.34**	**−0.38**
Mo	−0.19	0.07	−0.14
Na	0.19	0.13	0.03
Nb	−0.01	−0.03	0.16
Nd	−0.07	−0.01	0.03
Ni	0.08	−0.16	0.12
P	−0.06	−0.06	0.11
S	−0.16	−0.19	−0.01
Sb	−0.18	**0.21**	−0.17
Se	−0.09	**−0.22**	**0.35**
Si	0.19	0.14	0.03
Sn	−0.10	0.07	−0.02
Sr	−0.09	0.11	−0.02
Ta	0.11	0.06	0.08
Te	−0.15	0.08	−0.04
Th	0.17	0.09	0.07
Ti	0.19	0.16	0.01
U_3O_8	−0.09	−0.17	0.11
W	**−0.23**	0.06	−0.11
Y	0.03	−0.02	0.06
Zr	**0.20**	0.17	0.01
Zn	−0.17	0.05	0.01

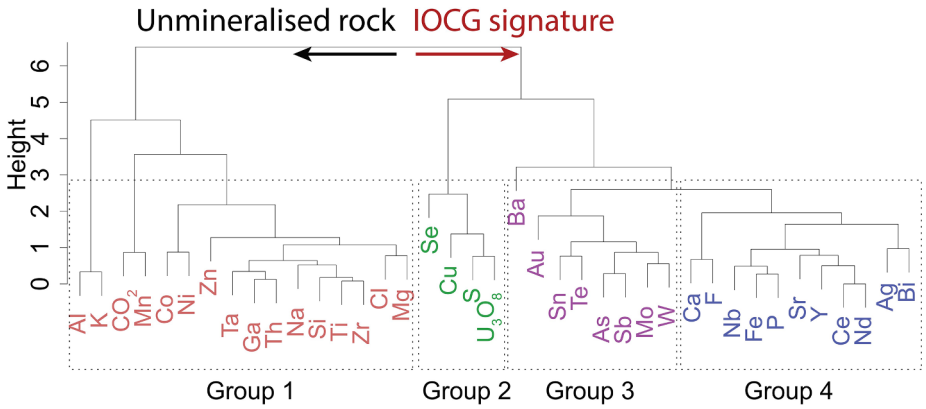

Fig. 3. Cluster dendrogram obtained from hierarchical cluster analysis of a 39-part geochemical sub-composition. The variation matrix (Appendix A; Table 2), which is based on pairwise logratios of the elements (Eq. (1)) , is used as a measure of dissimilarity.

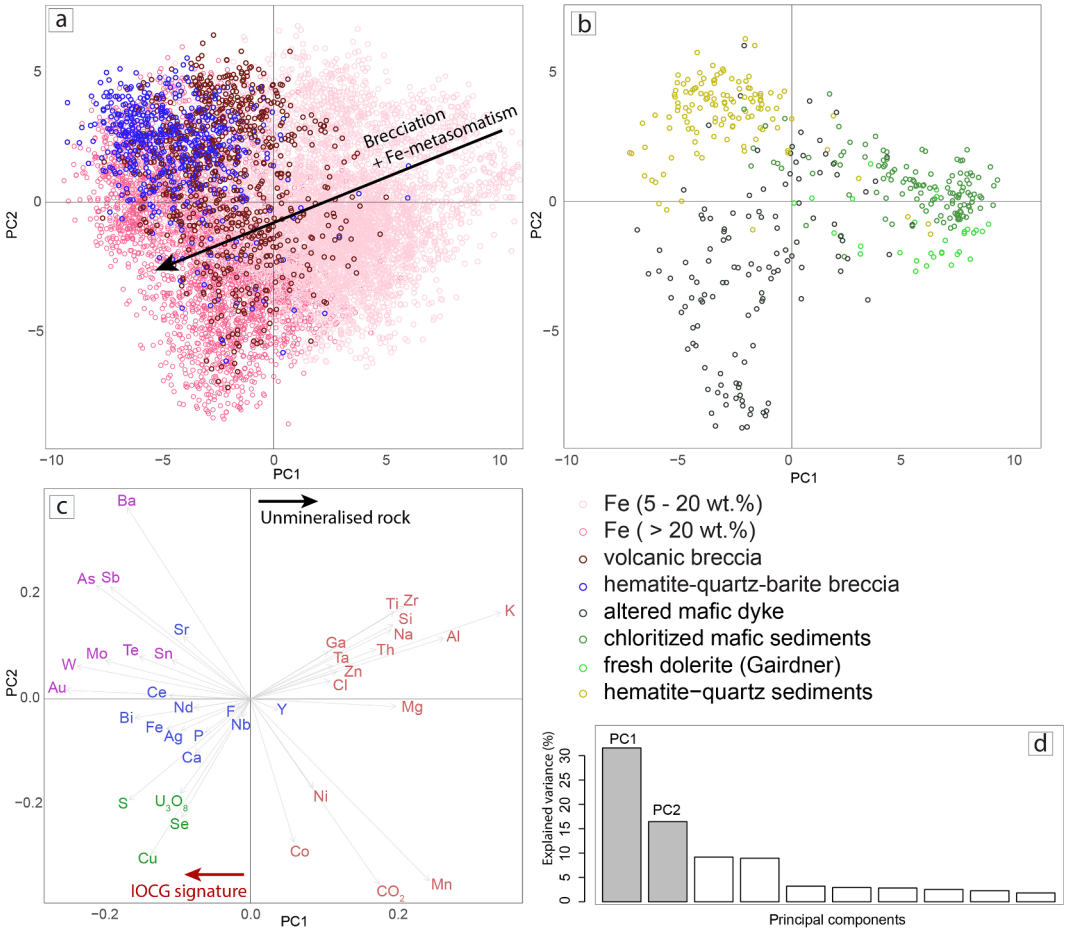

Fig. 4. The projected principal component scores of clr-transformed whole-rock data showing the dominant (a) and minor (b) lithological classes within the data (as in Table 1). Each data point represents a single sample. The principal component loadings (c) are color-coded to draw a comparison with the hierarchical dendrogram (Fig. 3). The scree plot illustrates the proportion of variance explained by each of the first ten principal components (d).

largest similarity with Ba. Finally, Group 4 encompasses a range of elements, including Ca, F, and REE (Ce and Nd) and the chalcophile elements Ag and Bi. The associations of elements presented in the dendrogram reflects the natural groups of elements mirrored by the combination of minerals.

4.2. Principal component analysis results

Principal component analysis of multi-element geochemical data after centred logratio transformation was used to examine relationship between elements in a 39-part sub-composition and reduce dimensionality.

The results of the PCA, including eigenvalues and loading of elements in PC1-3 are listed in Table 3. The graphs of the PC1-PC2 scores are split into two sub-charts to enhance the interpretability and visualization of the data. The biplot of PC1 and PC2 captures 31% and 16% of the total variation of the data, respectively (Fig. 4d). Because the sub-composition consists of both major and trace elements it is, therefore, assumed to reflect the major lithogeochemical variability, alteration patterns and geochemical affinities of trace elements. The PC1 is characterized by high positive loadings of K and Al. Both elements are largely hosted in RDG-derived K-feldspar, as well as in sericite and chlorite (the products of hydrothermal alteration of K-feldspar and micas). Elements associated with the mineralization in the ODBC, i.e., the IOCG-signature, appear on the opposite side of PC1; the largest loadings correspond to the association Au-W-Mo-As-Sb. The biplot (Fig. 4c) displays the multi-element associations of: (1) Ni-Co; (2) CO_2-Mn; (3) Zr-Th-Ti-Si-Na; (4) Cu-S-Se-U_3O_8; and (5) an element group comprising Ba, Sb, As, Mo, W and Au. We note that the element loadings displayed by PCs show subgroups of elements comparable to those suggested by the hierarchical cluster dendrogram (Fig. 3).

The two dominant sub-classes of hematite breccias, 5–20% and > 20% Fe, display a gradational change in whole-rock chemistry (Fig. 4a), whereas the least altered samples are those that show an association with granite-derived elements (e.g., K, Al and Si). In contrast, the whole-rock chemistry of breccias containing volcanic-clasts varies less, however this lithology is firmly tied to elements of Groups 1, 2 and 3 defining the IOCG signature.

Certain lithological classes display delineated clusters when plotted in PC1-PC2 space. Fresh dolerite and chloritized mafic sediments show a whole-rock chemistry that is distinct from that of altered mafic units. The latter stands out by the positive association with Group 2 elements. Quartz-baryte-bearing breccias, which is relatively depleted in Cu and U, are closely comparable with hematite-quartz sediments (Fig. 4a, b). The close resemblance between quartz-baryte-bearing breccia and hematite-quartz sediments is also underpinned by a correlation with the geochemical signature of the Ba, As, Sb, W, Mo and Au.

Based on the PCA results, a selection of groups of elements positively and inversely associated with the IOCG signature is presented below. These elements are split into groups and interpolated for each of the three sections, AA', BB' and CC'.

4.3. Delimitation of the ODBC from Roxby Downs Granite

The outline of the ODBC is defined by the logratio of K to Al, the distribution of PC1 scores, an isoline of Fe 20%, and the distribution of

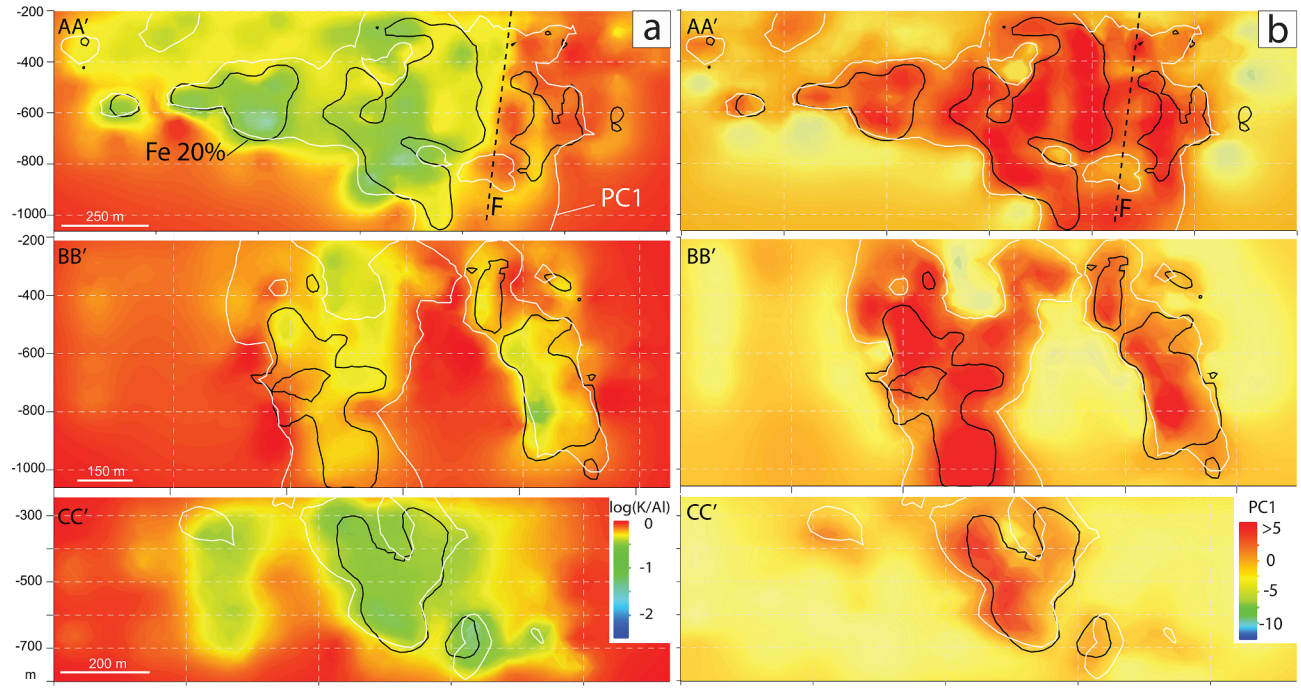

Fig. 5. Cross-sections AA', BB' and CC' illustrating kriged values of log-transformed molar ratio of K to Al (a) and PC1 scores derived from clr-transformed data (b). The kriged values are overlaid by isolines of 20 wt% Fe and PC1 scores that equal to zero.

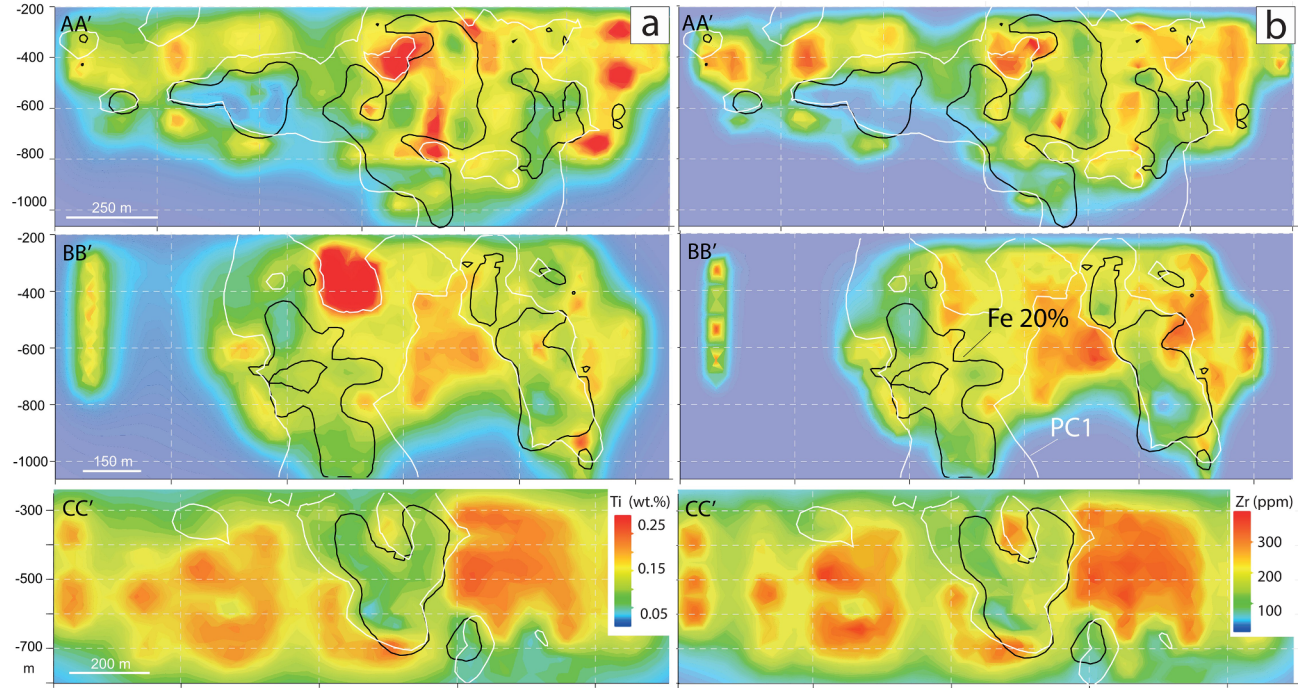

Fig. 6. Cross-sections AA', BB' and CC' showing the spatial distribution of Ti (in wt%) (a) and Zr (in ppm) (b) with an overlay of isolines of 20 wt% Fe and PC1 = zero.

Ti and Zr (Figs. 5 and 6). The logratio of K to Al maps out the extension of K-alteration enveloping the ODBC, while exhibiting the compositional variations of K and Al-bearing minerals (K-feldspar and sericite). Averaged out on the 15 m-interval whole-rock data, this logratio corresponds to the stoichiometry of K-feldspar if the logratio is equal to zero (Fig. 5a).

Similarly, the outline of ODBC is given by the kriged values of the PC1 scores, which are assigned to every sample in the dataset (Fig. 5b). In analogy with a clr-biplot, where principal component scores are displayed in two dimensions (Fig. 4a, b), the interpolation of scores in three dimensions allows investigation of their spatial distributions. An outline of PC1 scores equalling zero accurately delineates the ODBC from its host rocks. Samples with a positive score on PC1, i.e., placed within the outline, correspond to a lithogeochemical signature of IOCG mineralization within the ODBC, and correspond to negative values of $ln\left(\frac{K}{Al}\right)$. Notably, areas characterized by an occurrence of chloritized mafic sediments (sections BB' and CC'; Fig. 2) are defined by negative $ln\left(\frac{K}{Al}\right)$ and PC1.

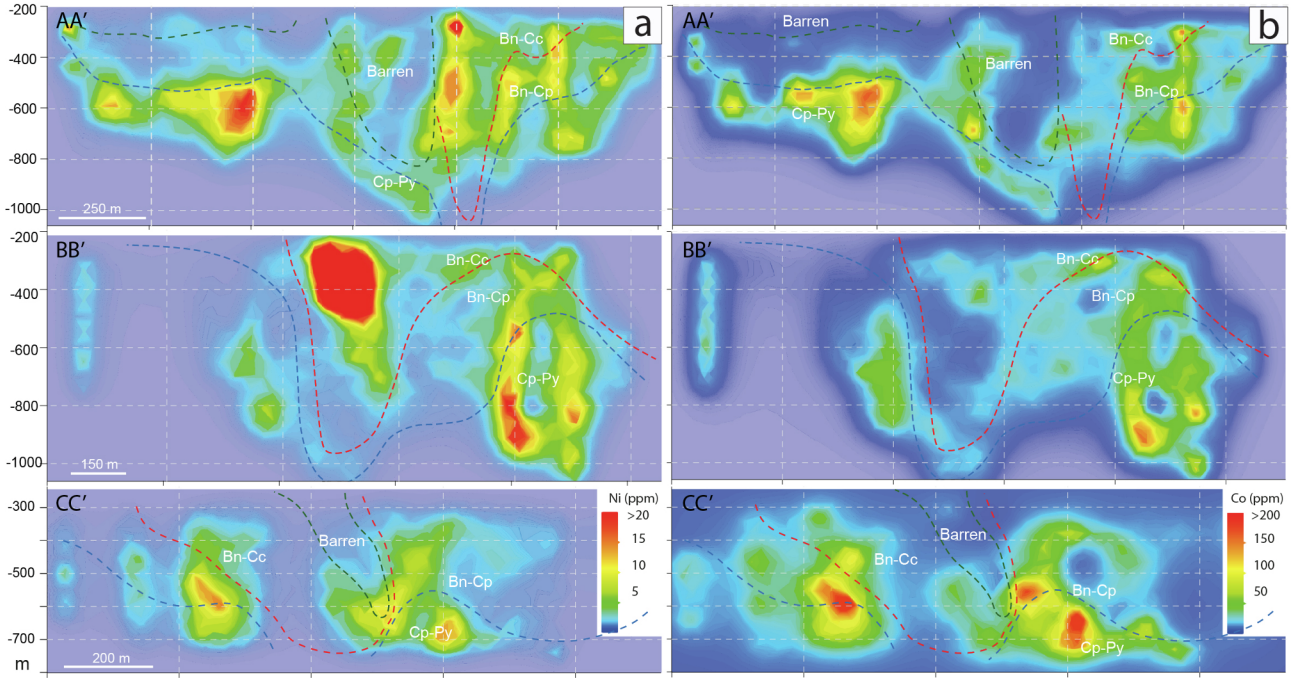

Fig. 7. Spatial distribution of (a) Ni and (b) Co (in ppm) in vertical cross-sections AA', BB' and CC'. The Cu(-Fe)-sulphide interfaces are estimates of modal mineralogy as in Fig. 2 (see Section 3.5).

The high field strength elements (HFSE), particularly, Ti and Zr, reflect the geochemical signature of the RDG (Figs. 4a, c and 6). The highest absolute concentrations of both elements occur outside the 20 wt% Fe outline and show an inverse association with Fe metasomatism in PC1, thus confirming that the ODBC is HFSE-depleted relative to the host granite. Furthermore, Ti points to the occurrences of mafic units, i.e., blocks of chloritized mafic sediments in shallower parts of section CC' and fresh Gairdner dolerite in section BB' (Fig. 6a).

4.4. Element distributions

4.4.1. Element pairs Ni-Co, Mn-CO_2 and Nb-Ta

Although Ni-Co and Mn-CO_2 fall within Group 1 on the dendrogram, these elements form an individual cluster observed in the PC1-PC2 projection (Fig. 4c). Such a slight yet noticable discrepancy could be attributed to the nature of these statistical analyses. The clustering algorithm partitions elements into the best possible homogenous groups by minimizing within-group similarities. On the other hand, PCA extracts the patterns that represent the highest variance in the data whereas it does not maximize the separation between the group.

Nickel and Co both show interrelation with Cu(-Fe)-sulphide zoning. Both elements are relatively enriched in the Py-Cp and Cp-Bn zones but are relatively depleted in the Bn-Cc zone (Fig. 7). Both elements can occur within pyrite and chalcopyrite, and as associated thiospinel and arsenic-sulphides of the arsenopyrite group, minerals which are rare or absent in bornite-chalcocite ores. Despite the significant spatial-geochemical similarities, the Ni-Co pair distribution has significant discrepancies that are attributed to zones of high-Ni and low-Co concentrations. These zones are specifically characterized by chloritized mafic sediments placed at shallow depths and as blocks in sections CC' and BB' (Fig. 7a).

The Mn-CO_2 pair displays a distribution resembling that of Ni-Co, but does not, however, correspond to Cu(-Fe)-zonation (Fig. 8). All four elements (Ni, Co, Mn and CO_2) typify the occurrences of fresh dolerite and altered mafic dykes, as for instance, in section BB', outside the positive PC1 values. In addition, these elements typify the occurrence of geochemical anomaly in volcanic and sericite-bearing hematite breccias in section CC' at a depth of ~800 m (Fig. 8). Despite the depletion in Group 3 elements (Au-W-Mo-Sb-As), this zone is placed within the PC1 values. Here, the pairs Ni-Co and Mn-CO_2 are highly correlated and correspond to samples containing Cu (~0.8 wt%) and U_3O_8 (~180 ppm) while showing an inverse association with Group 3 elements.

As revealed by the PCA, the ODBC exhibits a considerable decoupling between Nb and Ta. Not only is the latter reflected in PC1 (Fig. 4c) but also in the sections displaying the element distributions. Tantalum is a granite-derived element mostly concentrated outside of the Fe > 20 wt% outline and does not contribute to the IOCG signature. In contrast, Nb belongs to Group 2 elements and is concentrated in high-Fe zones, and especially in the altered mafic dyke from section AA' and at depth in section BB' (Fig. 9). Despite the strong decoupling of the two elements at higher concentrations, modest concentrations of Nb (up to 50 ppm) show patterns similar to Ta.

4.4.2. The U_3O_8-Se association

Group 2 contains the element pair U_3O_8-Se, which are closely associated as shown by the biplot, dendrogram, and variation matrix (Table 2). Group 2 is clearly related to the IOCG signature, as defined by PC1, but also displays a correlation with the granitophile elements. Notably, low U values, up to 200 ppm, are spatially correlated with granitophile elements (Figs. 10a and 11a–c). However, certain lithologies, such as quartz-baryte bearing breccias, appear relatively depleted in U despite being enriched in granitophile elements (Fig. 10a).

Despite U showing a good overlap with the Fe 20 wt% outline, high U values also exist outside the Fe contour, as seen in upper parts of section CC' and also section AA' (Fig. 10a). Notably, in the NW arm, U does not show an association with Fe metasomatism and even features relatively high values of 300 ppm on the eastern areas of AA' (Fig. 10a). As seen from cross-sections, U is strongly associated with Se although there are discrepancies in some areas, as for example, the high Se concentrations outside the IOCG outline (section CC'; Fig. 10b). In general, these elements are depleted in quartz-baryte bearing breccias in the central part of section BB' and also in chloritized mafic sediments (section CC'; Fig. 10).

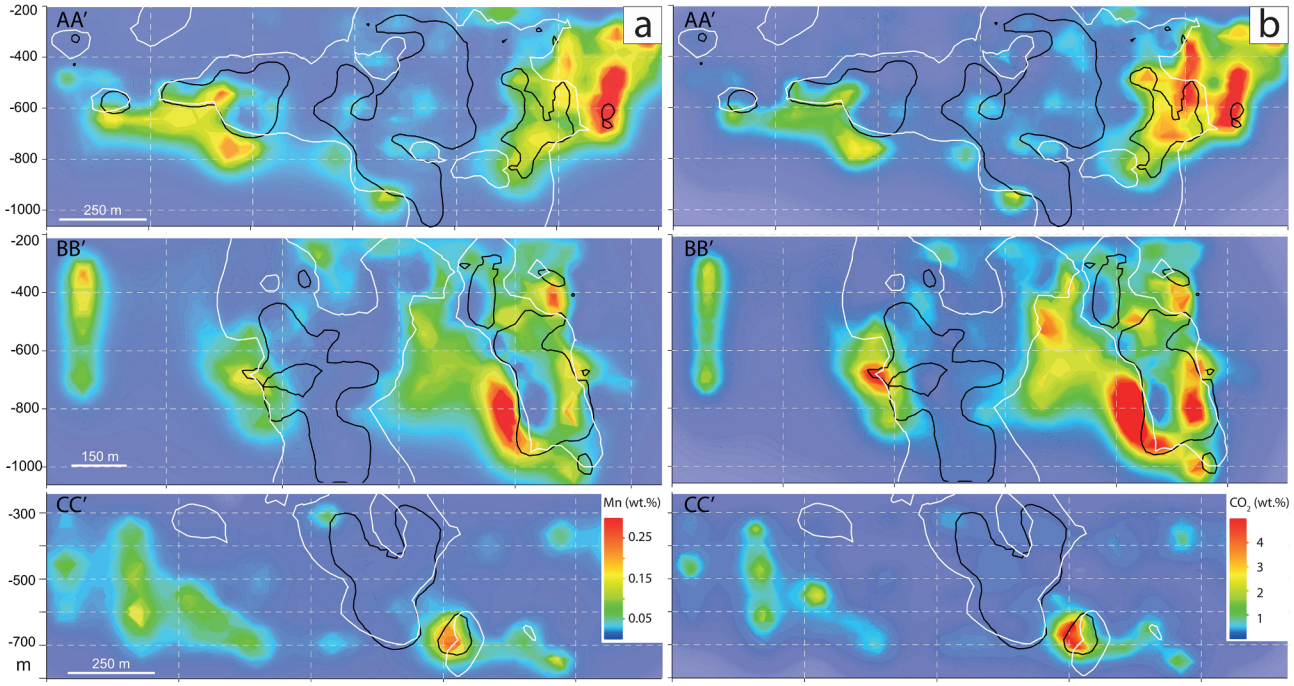

Fig. 8. Spatial distribution of (a) Mn and (b) CO_2 (in wt%) in cross-sections AA', BB' and CC' with overlay of 20 wt% Fe and PC1 = zero. Note the Mn-CO_2 geochemical anomaly in BB' at 800 m depth.

4.4.3. Granitophile elements (W-Sn-Mo)

Granitophile elements show close spatial-geochemical similarities as given by both PCA and the hierarchical dendrogram. Group 3 is specifically characterised by a lack of correlation with chloritized mafic sediments (Fig. 4b, c) and displays a strong relationship with Fe-metasomatism.

The granitophile elements, W, Sn and Mo, are ubiquitous throughout the ODBC and are consistently measurable above minimum limits of detection. Tungsten and Mo show a significant association with each other (τ_{WMo} = 0.6; Table 2), which is reflected in their spatial distributions. In contrast, the element pairs Sn and Mo (τ_{SnMo} = 1.1), and Sn and W (τ_{SnW} = 0.9) are slightly less associated although they still exhibit a remarkable spatial correlation (Fig. 11). Such a feature may be attributed to chalcopyrite, which is recognized as a systematic carrier of Sn (Ciobanu, 2015), whereas Mo and W are largely contained within hematite. Despite this, the absolute concentrations of granitophile elements are strongly linked to Fe-metasomatism and are thus always placed within the 20% Fe and PC1 outlines. This is readily reconciled by

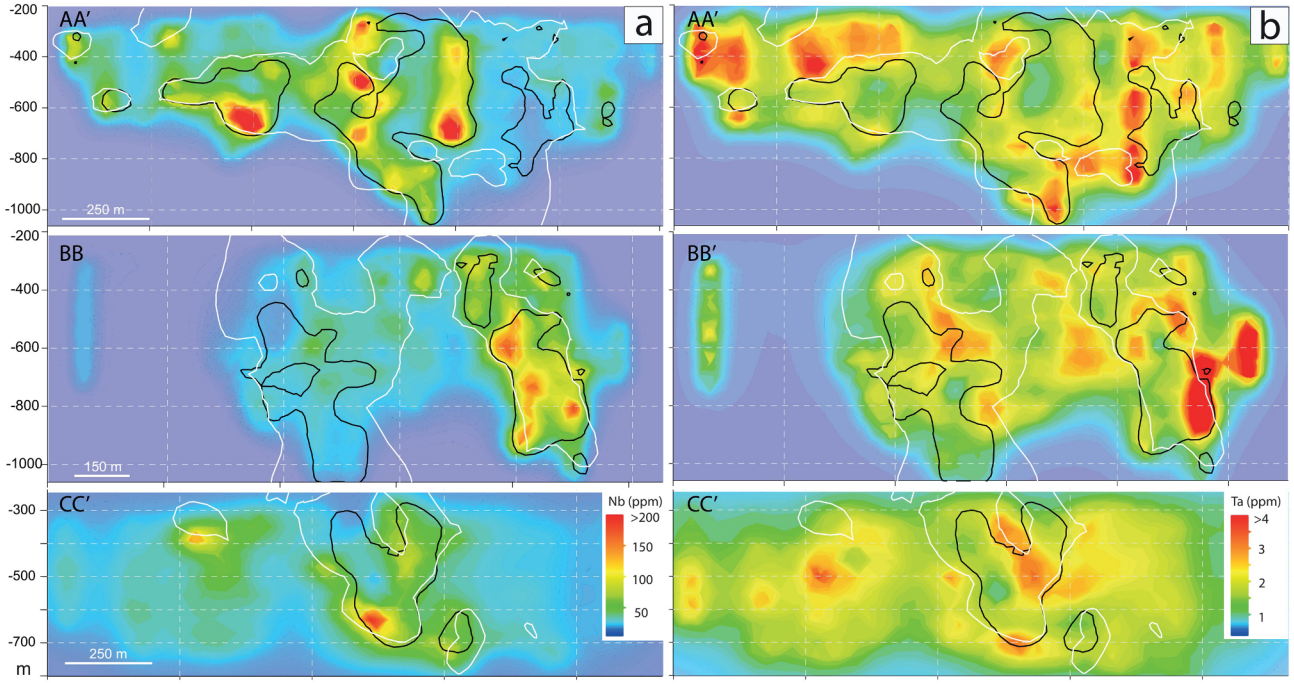

Fig. 9. The distribution of (a) Nb and (b) Ta (in ppm) in vertical cross-sections AA', BB' and CC' with the 20 wt% Fe and PC1 = zero isolines. Note the positive Ta anomalies outside of the PC1 = zero outline.

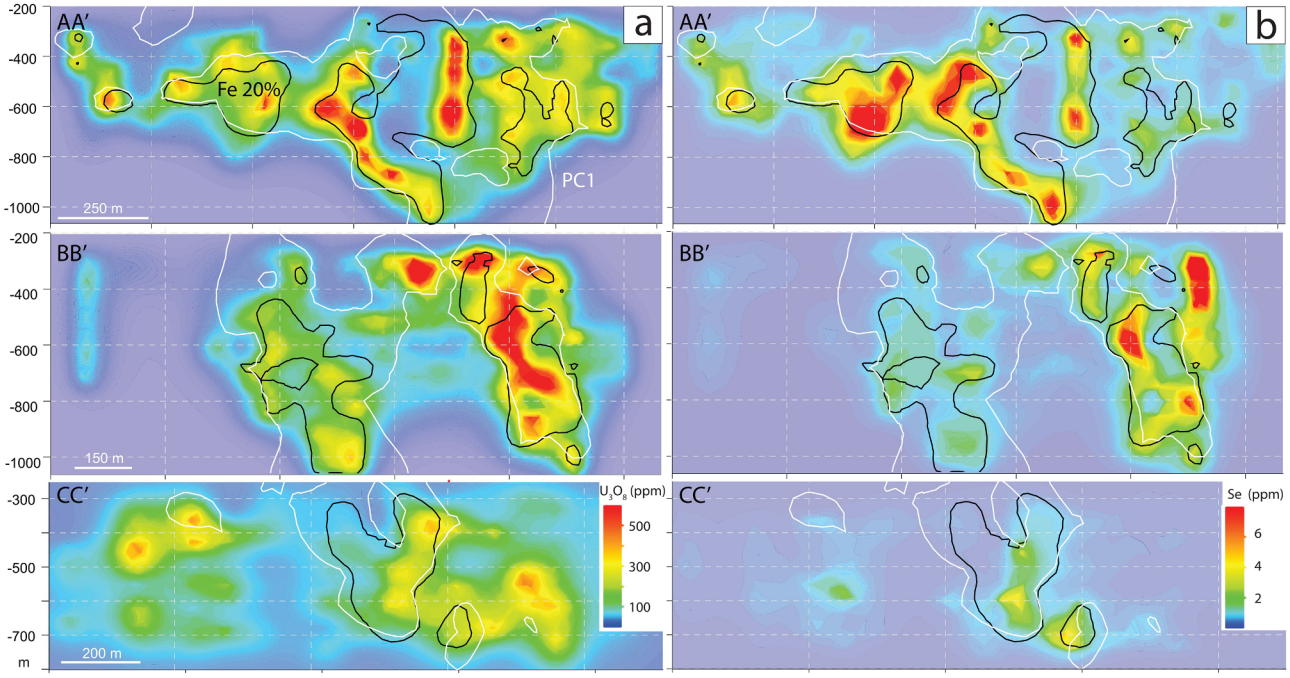

Fig. 10. Vertical cross-sections AA', BB' and CC' showing the distribution of (a) U_3O_8 and (b) Se (in ppm) with an overlay of 20 wt% Fe and PC1 = zero. Note the significant spatial correlation between U_3O_8 and Se.

the fact that these elements are almost exclusively hosted within hematite. The highest absolute concentrations of all granitophile elements are within drillhole RD1988 in the deepest part of section CC' (below 1400 m) and in the adjacent drillholes RD1999 and RD1960. In contrast, section AA' from the NW arm features local enrichment of granitophile elements at shallow levels and only very minor concentrations at depth (Fig. 11).

4.4.4. Chalcophile and related elements (As-Sb and Au-Te)

Although expected, the chalcophile elements Ag and Bi do not display a significant spatial correlation with one another. The cross-sections (Fig. 12) do not resolve a vertical zonation with respect to Ag and Bi, which contrasts with Ni-Co (showing a strong affiliation to the Py-Cp zone). Silver and Bi are present in all Cu-(Fe)-sulphide zones. Notably, both elements show a relative depletion in the quartz-hematite-bearing breccia (section AA'), and also in chlorite-bearing mafic sediments.

The other element pairs falling within Group 3 (As-Sb and Au-Te) are reasonably proportional, $\tau_{AsSb} = 0.4$ and $\tau_{AuTe} = 1.5$ (Table 2), thus exhibiting spatial correlation (section CC'; Figs. 13-14). All four elements are linked to Fe-metasomatism and correlate strongly with the granitophile elements, as seen in section CC', which shows enrichment in granitophile elements and As-Sb-Au-Te along the vertical mineralized corridor placed within the PC1 outline (Figs. 11, 13 and 14). However, Au is somewhat anomalous in that it displays low concentration in zones corresponding to quartz-baryte-bearing hematite breccias (section BB'; Fig. 14a). Nonetheless, shallow parts of the northern side of section AA' display relative enrichment in As and Te while showing high PC1 values and low Fe content (Figs. 13a and 14b). In the NW arm (section CC', Figs. 13 and 14), As-Sb and Au-Te, like the granitophile elements, show enrichment at shallow depths.

5. Discussion

5.1. Definition of an IOCG signature through PCA

Although the mineralogy of the OD deposit is well-characterised (Ehrig et al., 2012, 2017, and references therein), the low resolution-spacing multi-element whole-rock dataset analysed here lacks direct petrographic and mineralogical information. Inferences about the trace abundance mineralogical composition of individual samples can be made without the use of the mineral liberation analysis modal mineralogy dataset. This is due to the direct relationship between patterns and trends within the bulk geochemical data with the corresponding stoichiometries of ore- and rock-forming minerals (Aitchison, 1999). Overall, the PC1 reflects the averaged stoichiometric transition from RDG to hematite-dominant breccias, and displays a close overlap with geochemical changes associated with Fe-metasomatism (Fig. 5). Such a transition, as given by PC1, defines the specific IOCG mineralisation signature of the ODBC.

In magmatic-hydrothermal IOCG systems, such a signature is expected to contain the element association of Fe, Cu and Au defining the commodities exploited from the deposit, and/or minor elements that are characteristically anomalous in IOCG systems, notably U, REE, Ag and Co, but also including a broad range of other trace elements (Barton, 2014). The obtained IOCG signature encompasses the expected range of metals (Fig. 4c; Table 3). Notably, the range of metals that contribute to the IOCG signature are comparable to those of typical Cu ± Au ± Mo porphyry systems (Berger et al., 2008), since the IOCG signature evidently contains Mo, Ag, Ba, As, Sb and Te alongside Cu and Au (Fig. 4c). Overall, ore-forming processes in porphyry and IOCG systems likely share many similarities, such as magmatic affinity and enrichment in Fe (Richards and Mumin, 2013), and therefore these ore deposits will display a comparable range of metals. The similarities between the two groups of ore systems is intimately linked to crustal-scale processes, i.e., subduction and crustal extension, and input of metals from deep crust with mafic/mantle input (Skirrow et al., 2007; Groves et al., 2010; Richards et al., 2017).

The PCA results recognise two distinct associations (Au-W-Mo-Sb-As and S-Cu-Se-U_3O_8; Fig. 4c) within the IOCG signature. These associations are readily explained by their different spatial distribution. The Au-W-Mo-As-Sb group is spatially correlated with hematite and volcanic breccias, especially at depths below 1200 m, as well as in generally shallow quartz-baryte-bearing breccias (Figs. 11b, c, 13, and 14a). Although measured throughout the ODBC above the limits of detection, these elements are concentrated over the entire ~1800 m vertical extent of the mineralization and remain open at depth. The

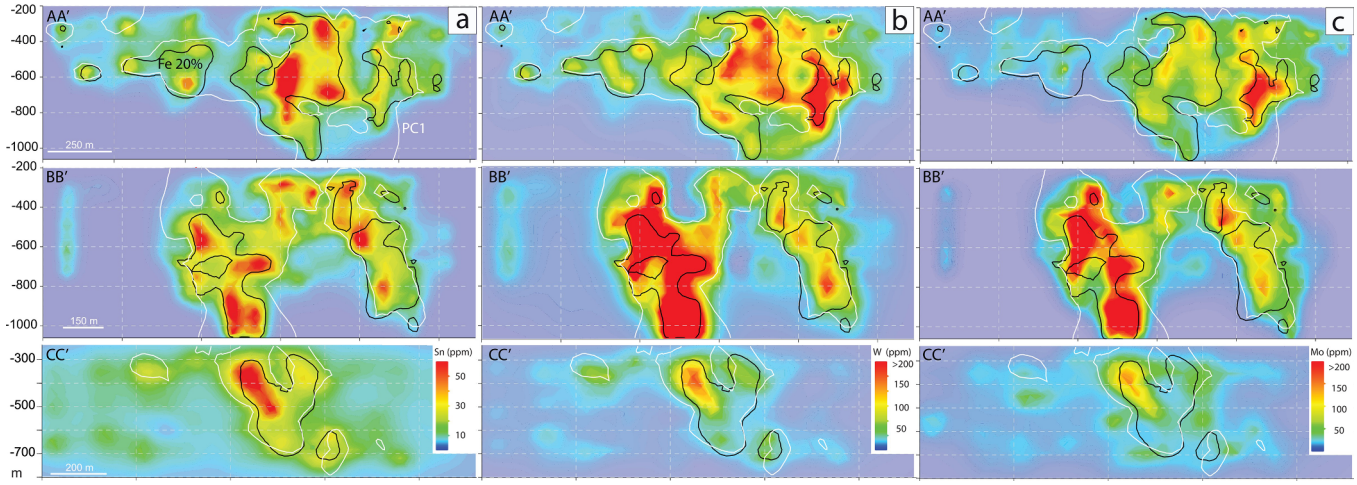

Fig. 11. The distribution of granitophile elements (a) Sn, (b) W, and (c) Mo in the vertical cross-sections AA', BB' and CC'. Note the great dependency of 20 wt% Fe outline and geochemical anomalies of granitophile elements.

concentration of elements along the vertical mineralized corridor is likely to be related to major structural feature such as a major subvertical WSW-ENE striking fault system (Fig. 1). On the other hand, the distribution of Cu mineralization, and to some extent also U, is known to be concentric (Ehrig et al., 2012), and as shown here, appears spatially independent from the Au-W-Mo-As-Sb association.

The Au-W-Mo-As-Sb signature can be attributed to a range of minerals, but is overwhelmingly related to compositionally-zoned hematite, which hosts most of the W, Mo and Sn throughout the deposit, as well as a significant part of the U (Verdugo-Ihl et al., 2017), and to sulphides hosting Sb and As: pyrite (As); tetrahedrite-tennantite (Sb-As); and cobaltite (As) (Ehrig et al., 2012). Gold is mostly in native form, alloyed with Ag (and rarely Cu), or as Au(± Ag)-tellurides, occurring as inclusions in sulphides and hematite.

Although mineral parageneses and ore-forming processes can only be inferred from whole rock data, the abundant body of metasomatic hematite endowed with W-Sn (± U-Mo) can be considered to represent a primary hydrothermal event in the ODBC. The Au-W-Mo-As-Sb association includes As, Sb and Au, elements which in some magmatic-hydrothermal systems (e.g., porphyry deposits) are considered as a shallow expression of mineralization (e.g., Richards and Mumin, 2013). Given that, we suggest the vertical 1800 m deep mineralized corridor anomalous in Au-W-Mo-As-Sb may represent a hydrothermal-fluid conduit. This is because the observed lithologies in the SE lobe (volcanic and sedimentary rocks) are all displaying the same IOCG signature and thus have been incorporated within the granite along a subvertical fault prior to, or during the onset of the mineralising system. On the other hand, the deep mineralized corridor may represent a subvertical fault system which hosts IOCG-signature bearing/mineralized breccias and sediments that were structurally incorporated into the ODBC from the shallower levels of the deposit. Thus, the occurrence of the mineralized corridor within a fault system may explain the geochemical signature documented along drillhole RD1988 which contains a wide variety of preserved, early paragenetic sequences

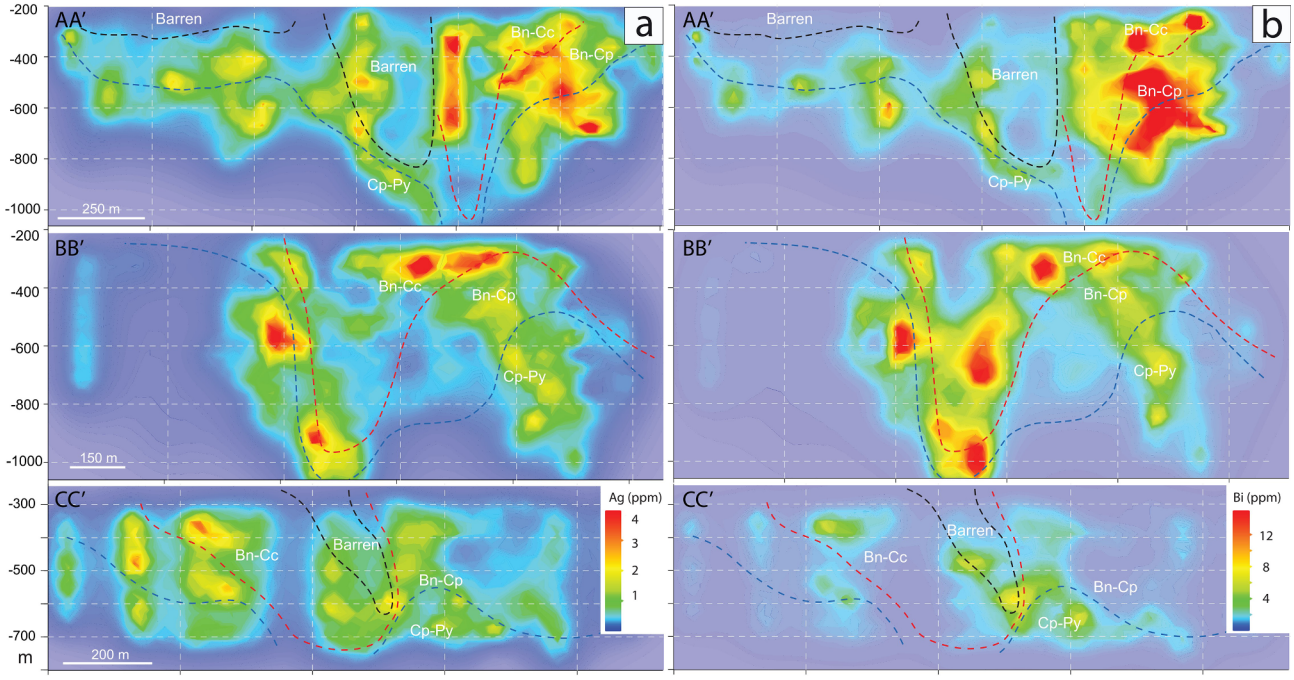

Fig. 12. Illustration of the vertical cross-sections AA', BB' and CC' showing the distributions of (a) Ag and (b) Bi with an overlay of interfaces of the estimated normative Cu-(Fe)-sulphide mineralogy (see Section 3.5).

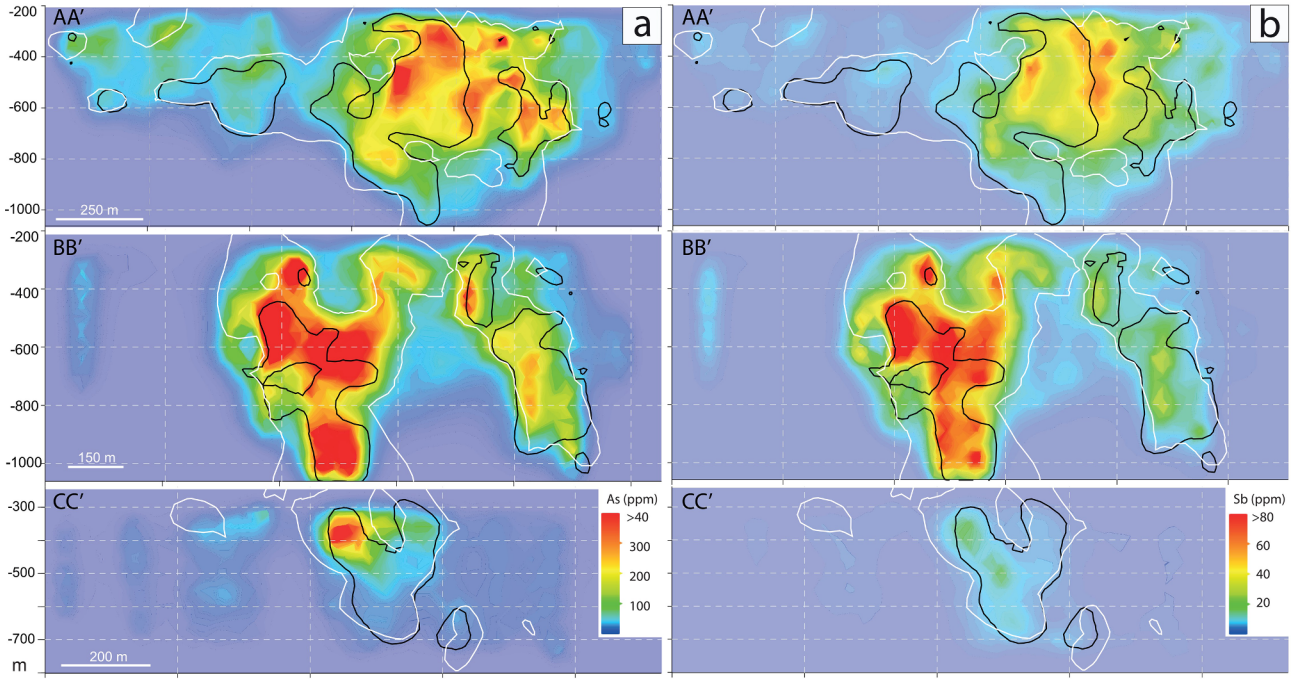

Fig. 13. Spatial distribution of (a) As and (b) Sb in vertical cross-sections AA', BB' and CC' with 20 wt% Fe and PC1 = zero outlines. Note the high spatial dependency between As and Sb geochemical anomalies and Fe-rich (> 20 wt%) zones.

combined with the expressions of superimposed multi-stage re-mobilization and redistribution of ore components. Overall, the Au-W-Mo-As-Sb association represents a significant pathfinder element group and is likely present in other IOCG deposits within the Olympic Cu-Au Province.

5.2. Lithogeochemistry of the Olympic Dam Breccia Complex

Although the extensive sampling grid covers the ODBC, no geochemical gradients could be recognised in PC1 other than those showing a match between certain breccia types/lithologies and the overall IOCG signature defined by the PC1 (Fig. 5b). Nevertheless, as shown here, the PCA is an effective tool to underpin multi-element signatures with lithological units.

Despite the close relationship between PC1 and > Fe 20 wt%, if compared to the cross-section (Fig. 5b), the distribution of positive PC1 values only partially overlaps with the distribution of > 20 wt% Fe hematite breccias and vice versa. This discrepancy may suggest that mineralization is not associated with Fe-metasomatism in some parts of the deposit. In turn it can be inferred that either (i) some sulphide accumulations do not coincide with Fe-metasomatism and represent the products of later sulphide remobilization, e.g., sulphide-rich veins on

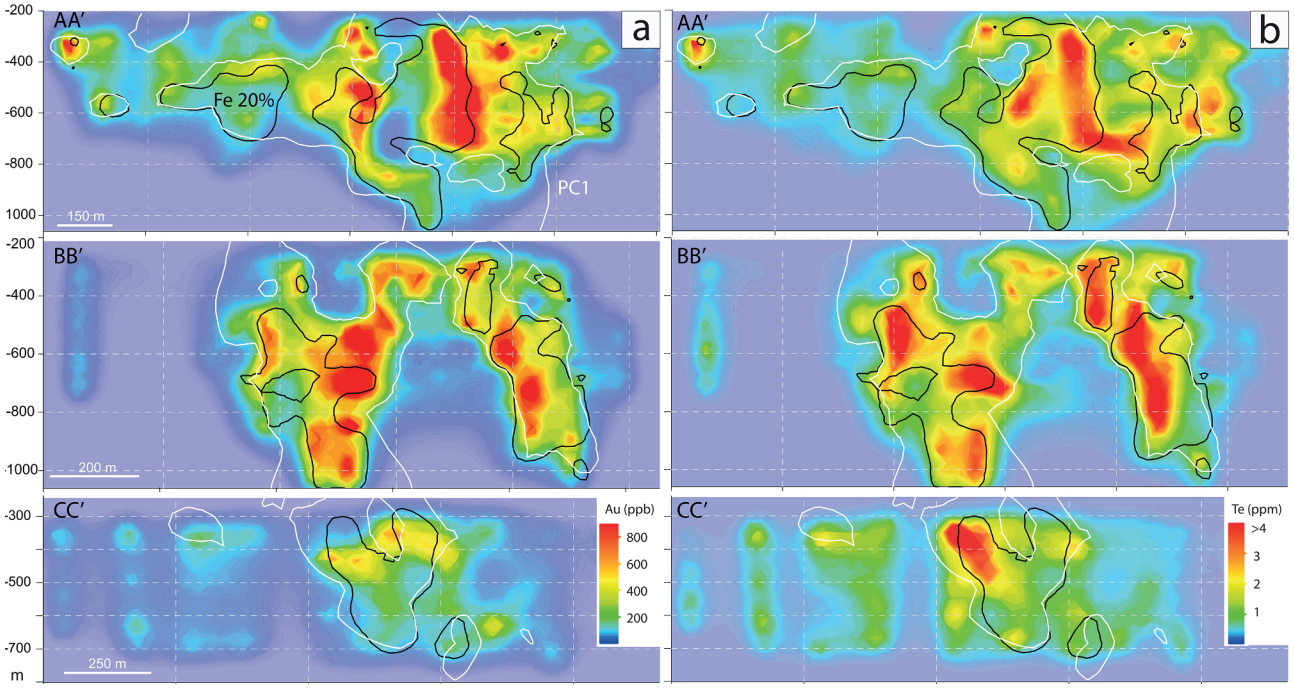

Fig. 14. Vertical cross-sections AA', BB' and CC' and corresponding distributions of (a) Au and (b) Te with an overlay of 20 wt% Fe and PC1 = zero.

the periphery of the ODBC in zones of only weak Fe-metasomatism, or (ii) that some Fe-rich pockets may pre- or postdate IOCG mineralization, e.g., preserved fragments of older Fe-rich sedimentary rocks. In addition, a distinct style of mineralization on the outer margins of the deposit, notably in the northwestern arm (Fig. 10a), may contribute to the observed discrepancy between PC1 and Fe.

The PC1 depicts the lack of IOCG signature in chlorite-bearing mafic sediments as given by the PC1-PC2 projection and the cross-sections (Fig. 5b). Although Cu-bearing minerals are present in chlorite-bearing mafic sediments (up to ~1.5 wt% Cu), the lack of an IOCG signature implies that the provenance of these sediments is unrelated to the IOCG mineralizing process. In contrast, hematite-quartz sediments are characterized by the IOCG signature. This may suggest that the latter sediments are partially sourced from ODBC rocks (McPhie et al., 2016), or nearby, eroded IOCG systems. Interestingly, altered mafic-ultramafic units, coeval with emplacement of RGD, within the ODBC also display IOCG signatures, and substantial enrichment in Cu and U. The latter supports the coeval bimodal magmatism immediately preceding initiation of hydrothermal activity that precipitated IOCG mineralization (Huang et al., 2016) (Fig. 5b).

5.3. Vertical zonation

Since the Cu-(Fe)-sulphides display vertical and lateral zonation, it is expected that certain chalcophile/siderophile elements should either reproduce such a zonation, or give additional gradients. Nickel and Co are closely associated with pyrite in the deeper pyrite-chalcopyrite parts of the ODBC (Fig. 7), in accordance with empirical observations of Ni- and Co-bearing minerals (pyrite, carrollite and cobaltite) within the Py-Cp zone (Ehrig et al., 2012). In contrast, the Bn-Cc zone features a relative depletion in Ni and Co at shallower depths (Fig. 7), corresponding to the low (often below minimum limits of detection) concentrations of Ni and Co in bornite and chalcocite (Ciobanu, 2015).

In contrast, Ag and Bi, are chalcophile elements and are readily partitioned into bornite (Bi > Ag) and chalcocite/digenite (Ag < Bi) (Cook et al., 2011). Therefore, Ag and Bi might be expected to display a relative enrichment at shallow levels within the ODBC. No such systematic patterns are, however, resolvable. Multiple explanations can be found for such discordance, possibly the most important being the sampling resolution, which may be inadequate to resolve the zonation in detail. Subordinate explanations include the presence of both Ag and Bi as discrete, sub-micron-scale inclusions of minor telluride and sulphosalt phases (e.g., hessite, tetradymite, wittichenite) in sulphides and other minerals throughout the deposit, and also the presence of Ag within chalcopyrite at depth in the absence of either chalcocite and bornite (Ciobanu, 2015).

5.4. Geochemical trends and associations

Oscillatory-zoned hematite, which is found throughout the 1800 m vertical extent of mineralization (Verdugo-Ihl et al., 2017), contains elevated concentrations of U, W, Sn and Mo. The same geochemical signature also occurs throughout the whole-rock samples in the ODBC, however, whole-rock data show a spatial separation between U and the remaining granitophile elements. As seen in Fig. 10a, concentrations of up to 200 ppm U correlate with W-Sn-Mo but that correlation diminishes at higher U concentrations. The three main U-bearing minerals are uraninite, brannerite and coffinite (Macmillan et al., 2016a, 2017), together accounting for ~80–85% of total U. These minerals are dispersed throughout the ODBC, occur as inclusions in hematite, sulphides and most other minerals, and also display extensive evidence of breakdown, replacement, remobilization and re-concentration (Macmillan et al., 2016a, 2017). Although these processes are readily recognizable in drillcore specimens and polished mounts, their scale and impact on deposit-scale U distributions are less well constrained and are only partially resolved by the whole-rock dataset. Moreover, the radioactive decay of U-bearing minerals and migration of daughter radionuclides and radiogenic lead is also observed at the scale of nanometres upwards (Rollog et al., 2019).

Analyses of the whole-rock data exhibit a remarkably strong U_3O_8-Se-Cu-S association throughout the ODBC (Fig. 10), in which Se and U_3O_8 are particularly strongly correlated. A partial explanation for such a trend is found within the preferential partitioning of Se into Cu(-Fe)-sulphides (e.g., Cook et al., 2011; George et al., 2016), where it substitutes for S. Selenide minerals are generally rare at OD but the most abundant of these, clausthalite (PbSe) can readily form via interaction between sulphide-hosted Se and remobilized radiogenic Pb as shown in other IOCG deposits from the Gawler Craton (Owen et al., 2018).

A further geochemical trend is attributed to the positive anomaly of CO_2, Mn, Co, Ni and Nb in section BB'. This zone, which is also mineralized and contains ~50 wt% Fe based on whole-rock data, differs significantly from the remaining data set. This is due to this association being attributed to a pyrite-magnetite-apatite-siderite assemblage which can be regarded as a geochemical signature specific to deep, peripheral, relatively-reduced Fe-oxide alteration.

6. Conclusions and outlook

Application of PCA and hierarchical clustering to large whole-rock data sets is an effective way to underpin spatio-geochemical associations and delineate an orebody in a disseminated mineral system. Recognition of multi-element geochemical signatures is important in the ODBC because despite the presence of generally common elements (Fe, Cu and Au), there are other accompanying indicator elements such as W, Mo, As and Sb. Trace elements contributing to the multi-element IOCG signature are likely to be common within other IOCG systems in the Olympic Cu-Au Province and can be utilized as vectors in near-mine exploration.

Further work should address IOCG signatures within prospects adjacent to OD displaying similar but not identical mineralization style, e.g., at Wirrda Well and Acropolis (Krneta et al., 2017), to understand the fundamental mineralogical, geochemical and genetic controls on trace element distribution patterns. Considerable opportunity therefore exists for testing whether granitophile signature are unique to the ODBC, or are ubiquitous throughout IOCG deposits of the Olympic Cu-Au Province, and potentially, also elsewhere.

The PC1 gives neither solid gradients nor defines zonation within the ODBC. Similarly, the individual trace element dispersion patterns within the ODBC cannot capture the zonation due to the low-resolution of the whole-rock data, complex partitioning patterns dependent on a range of factors, and superimposed processes that have modified primary distribution patterns. Therefore, considering the complexity of ore assemblages in response to multiple episodes of mineral dissolution and (re)precipitation, trace element signatures in individual minerals, e.g., Cu(-Fe)-sulphides, or Fe-oxides, may prove more efficient at constraining the spatiotemporal evolution of the ODBC. The variations in trace element signatures in individual minerals may provide systematic geochemical tracers that can be interpreted in terms of prograde and retrograde hydrothermal fluid evolution. Such an approach, if coupled with careful textural and compositional characterisation of relevant minerals, can be used to define vertical/lateral zonation to underpin the evolution of the system in space and time.

Acknowledgments

This work is a contribution to the FOX project 'Trace elements in iron-oxides: deportment, distribution and application in ore genesis, geochronology, exploration and mineral processing', supported by BHP Olympic Dam and the South Australian Mining and Petroleum Services Centre of Excellence. N.J.C. acknowledges additional support from the ARC Research Hub for Australian Copper-Uranium (Grant IH130200033). Constructive comments from an anonymous reviewer

and Editor-in-Chief Franco Pirajno are highly appreciated.

Appendix A. Supplementary data

Supplementary data to this article can be found online at https://doi.org/10.1016/j.oregeorev.2018.12.013.

References

Aitchison, J., 1986. The statistical analysis of compositional data. Monographs on Statistics and Applied Probability. Chapman & Hall, London http://dx.doi.org/10.1007/978-94-009-4109-0.

Aitchison, J., 1999. Logratios and natural laws in compositional data analysis. Math. Geol. 31, 563–580. https://doi.org/10.1023/A:1007568008032.

Allen, S.R., McPhie, J., Ferris, G., Simpson, C., 2008. Evolution and architecture of a large felsic Igneous Province in western Laurentia: the 1.6 Ga Gawler Range Volcanics, South Australia. J. Volcanol. Geotherm. Res. 172, 132–147. https://doi.org/10.1016/j.jvolgeores.2005.09.027.

Apukhtina, O.B., Kamenetsky, V.S., Ehrig, K., Kamenetsky, M.B., Maas, R., Thompson, J., McPhie, J., Ciobanu, C.L., Cook, N.J., 2017. Early, deep magnetite-fluorapatite mineralization at the Olympic Dam Cu-U-Au-Ag deposit, South Australia. Econ. Geol. 112, 1531–1542. https://doi.org/10.5382/econgeo.2017.4520.

Barton, M.D., 2014. Iron oxide (–Cu–Au–REE–P–Ag–U–Co) systems. In: Holland, H.D., Turekian, K.K. (Eds.), Treatise on Geochemistry,, second ed. Elsevier, Oxford, pp. 515–541 https://doi.org/10.1016/B978-0-08-095975-7.01123-2.

Berger, B.R., Ayuso, R.A., Wynn, J.C., Seal, R., 2008. Preliminary model of porphyry copper deposits. In: USGS Numbered Series Open-file Report, pp. 55 https://doi.org/10.3133/ofr20081321.

Chen, S., Hattori, K., Grunsky, E.C., 2017. Multielement statistical evidence for uraniferous hydrothermal activity in sandstones overlying the Phoenix uranium deposit, Athabasca Basin, Canada. Mineral. Deposita 53, 493–508. https://doi.org/10.1007/s00126-017-0756-2.

Cherry, A., Ehrig, K., Kamenetsky, V.S., McPhie, J., Crowley, J., Kamenetsky, M., 2018. Precise geochronological constraints on the origin, setting and incorporation of ca. 1.59 Ga surficial facies into the Olympic Dam Breccia Complex, South Australia. Precambr. Res. 315, 162–168. https://doi.org/10.1016/j.precamres.2018.07.012.

Ciobanu, C.L., 2015. Trace element signatures in sulphides at Olympic Dam and satellite prospects: a reconnaissance study for ore vectoring using Cu-(Fe)-sulphides in Iron Oxide Copper Gold Deposits. Unpublished Report. The University of Adelaide.

Ciobanu, C.L., Wade, B.P., Cook, N.J., Schmidt Mumm, A., Giles, D., 2013. Uranium-bearing hematite from the Olympic Dam Cu-U-Au deposit, South Australia: a geochemical tracer and reconnaissance Pb-Pb geochronometer. Precambr. Res. 238, 129–147. https://doi.org/10.1016/j.precamres.2013.10.007.

Ciobanu, C.L., Cook, N.J., Ehrig, K., 2017. Ore minerals down to the nanoscale: Cu-(Fe)-sulphides from the iron oxide copper gold deposit at Olympic Dam, South Australia. Ore Geol. Rev. 81, 1218–1235. https://doi.org/10.1016/j.oregeorev.2016.08.015.

Conor, C., Raymond, O., Baker, T., Teale, G., Say, P., Lowe, G., 2010. Alteration and mineralisation in the Moonta-Wallaroo Cu–Au mining field region, Olympic domain, South Australia. In: Porter, M. (Ed.), Hydrothermal Iron Oxide Copper-Gold and Related Deposits: A Global Perspective 3. PGC Publishing, Adelaide, pp. 1–24.

Cook, N.J., Ciobanu, C.L., Danyushevsky, L.V., Gilbert, S., 2011. Minor and trace elements in bornite and associated Cu–(Fe)-sulfides: a LA-ICP-MS study. Geochim. Cosmochim. Acta 75, 6473–6496. https://doi.org/10.1016/j.gca.2011.08.021.

Creaser, R.A., 1989. The Geology and Petrology of Middle Proterozoic Felsic Magmatism of the Stuart Shelf, South Australia. Unpublished Ph.D. thesis. La Trobe University, Melbourne, Australia.

Ehrig, K., McPhie, J., Kamenetsky, V., 2012. Geology and mineralogical zonation of the olympic dam iron oxide Cu-U-Au-Ag deposit, South Australia. Soc. Econ. Geol. Spec. Pub. 16, 237–267.

Ehrig, K., Kamenetsky, V., McPhie, J., Cook, N.J., Ciobanu, C.L., 2017. Olympic Dam iron-oxide Cu-U-Au-Ag deposit. In: Phillips, G.N. (Ed.), Australian Ore Deposits. AusIMM, Melbourne, pp. 601–610.

Gabriel, K.R., 1971. The biplot graphical display of matrices with application to principal component analysis. Biometrika 58, 453–467. https://doi.org/10.1093/biomet/58.3.453.

George, L.L., Cook, N.J., Ciobanu, C.L., 2016. Partitioning of trace elements in co-crystallized sphalerite–galena–chalcopyrite hydrothermal ores. Ore Geol. Rev. 77, 97–116.

Groves, D.I., Bierlein, F.P., Meinert, L.D., Hitzman, M.W., 2010. Iron Oxide Copper-Gold (IOCG) deposits through earth history: implications for origin, lithospheric setting, and distinction from other epigenetic iron oxide deposits. Econ. Geol. 105, 641–654. https://doi.org/10.2113/gsecongeo.105.3.641.

Grunsky, E., 2010. The interpretation of geochemical survey data. Geochem. Explor. Env. A. 10, 27–74. https://doi.org/10.1144/1467-7873/09-210.

Grunsky, E., Mueller, U.A., Corrigan, D., 2014. A study of the lake sediment geochemistry of the Melville Peninsula using multivariate methods: applications for predictive geological mapping. J. Geochem. Explor. 141, 15–41. https://doi.org/10.1016/j.gexplo.2013.07.013.

Guilbert, J.M., Park, C.F., 1986. The Geology of Ore Deposits. W.H. Freeman and Co, London, pp. 985.

Helsel, D., 2006. Fabricating data: How substituting values for nondetects can ruin results, and what can be done about it. Chemosphere 65, 2434–2439. https://doi.org/10.1016/j.chemosphere.2006.04.051.

Hitzman, M.W., Oreskes, N., Einaudi, M.T., 1992. Geological characteristics and tectonic setting of Proterozoic iron oxide (Cu-U-Au-REE) deposits. Precambr. Res. 58, 241–287. https://doi.org/10.1016/0301-9268(92)90121-4.

Huang, Q., Kamenetsky, V.S., McPhie, J., Ehrig, K., Meffre, S., Maas, R., Thompson, J., Kamenetsky, M., Chambefort, I., Apukhtina, O., Hu, Y., 2015. Neoproterozoic (ca. 820–830 Ma) mafic dykes at Olympic Dam, South Australia: links with the Gairdner Large Igneous Province. Precambr. Res. 271, 160–172. https://doi.org/10.1016/j.precamres.2015.10.001.

Huang, Q., Kamenetsky, V.S., Ehrig, K., McPhie, J., Kamenetsky, M., Cross, K., Meffre, S., Agangi, A., Chambefort, I., Direen, N.G., Maas, R., Apukhtina, O., 2016. Olivine-phyric basalt in the Mesoproterozoic Gawler silicic large igneous province, South Australia: examples at the Olympic Dam Iron Oxide Cu–U–Au–Ag deposit and other localities. Precambr. Res. 281, 185–199. https://doi.org/10.1016/j.precamres.2016.05.019.

Ismail, R., Ciobanu, C.L., Cook, N.J., Teale, G.S., Giles, D., Schmidt Mumm, A., Wade, B., 2014. Rare earths and other trace elements in minerals from skarn assemblages, Hillside iron oxide–copper–gold deposit, Yorke Peninsula, South Australia. Lithos 184–187, 456–477. https://doi.org/10.1016/j.lithos.2013.07.023.

Kontonikas-Charos, A., Ciobanu, C.L., Cook, N.J., 2014. Albitization and redistribution of REE and Y in IOCG systems: insights from Moonta-Wallaroo, Yorke Peninsula, South Australia. Lithos 208–209, 178–201. https://doi.org/10.1016/j.lithos.2014.09.001.

Kontonikas-Charos, A., Ciobanu, C.L., Cook, N.J., Ehrig, K., Krneta, S., Kamenetsky, V.S., 2017. Feldspar evolution in the Roxby Downs Granite, host to Fe-oxide Cu-Au-(U) mineralisation at Olympic Dam, South Australia. Ore Geol. Rev. 80, 838–859. https://doi.org/10.1016/j.oregeorev.2016.08.019.

Krneta, S., Ciobanu, C.L., Cook, N.J., Ehrig, K., Kontonikas-Charos, A., 2016. Apatite at Olympic Dam, South Australia: a petrogenetic tool. Lithos 262, 470–485. https://doi.org/10.3390/min8080342.

Krneta, S., Ciobanu, C.L., Cook, N.J., Ehrig, K., Kontonikas-Charos, A., 2017. The Wirrda Well and Acropolis prospects Gawler Craton, South Australia: insights into evolving fluid conditions through apatite chemistry. J. Geochem. Explor. 181, 276–291. https://doi.org/10.1016/j.gexplo.2017.08.004.

Macmillan, E., Cook, N.J., Ehrig, K., Ciobanu, C.L., Pring, A., 2016a. Uraninite from the Olympic Dam IOCG-U-Ag deposit: linking textural and compositional variation to temporal evolution. Am. Mineral. 101, 1295–1320. https://doi.org/10.2138/am-2016-5411.

Macmillan, E., Ciobanu, C.L., Ehrig, K., Cook, N.J., Pring, A., 2016b. Chemical zoning and lattice distortion in uraninite from Olympic Dam, South Australia. Am. Mineral. 101, 2351–2354. https://doi.org/10.1180/minmag.2017.081.006.

Macmillan, E., Ehrig, K., Ciobanu, C.L., Cook, N.J., Pring, A., 2016c. Replacement of uraninite by bornite via coupled dissolution-reprecipitation: evidence from texture and microstructure. Can. Mineral. 54, 1369–1383. https://doi.org/10.3749/canmin.1600031.

Macmillan, E., Cook, N.J., Ehrig, K., Pring, A., 2017. Chemical and textural interpretation of late-stage coffinite and brannerite from the Olympic Dam IOCG-Ag-U deposit. Mineral. Mag. 81, 1323–1366. https://doi.org/10.1180/minmag.2017.081.006.

Mark, G., Oliver, N.H.S., Williams, P.J., 2006. Mineralogical and chemical evolution of the Ernest Henry Fe-oxide-Cu-Au ore system, Cloncurry district, northwest Queensland, Australia. Mineral. Deposita 40, 769–801. https://doi.org/10.1007/s00126-005-0009-7.

Mauger, A.J., Ehrig, K.J., Kontonikas-Charos, A., Ciobanu, C.L., Cook, N.J., Kamenetsky, V.S., 2016. Alteration at the Olympic Dam IOCG–U deposit: insights into distal to proximal feldspar and phyllosilicate chemistry from infrared reflectance spectroscopy. Austral. J. Earth Sci. 63, 959–972. https://doi.org/10.1080/08120099.2016.1264474.

McPhie, J., Orth, K., Kamenetsky, V., Kamenetsky, M., Ehrig, K., 2016. Characteristics, origin and significance of Mesoproterozoic bedded clastic facies at the Olympic Dam Cu–U–Au–Ag deposit, South Australia. Precambr. Res. 276, 85–100. https://doi.org/10.1016/j.precamres.2016.01.029.

Meinert, L., 1997. Application of skarn deposit zonation models to mineral exploration. Explor. Min. Geol. 6, 185–208.

Oliver, N.H.S., Cleverley, J.S., Mark, G., Pollard, P.J., Fu, B., Marshall, L.J., Rubenach, M.J., Williams, P.J., Baker, T., 2004. The role of sodic alteration in the genesis of iron oxide-copper-gold deposits, eastern Mt Isa Block, Australia. Econ. Geol. 99, 1145–1176. https://doi.org/10.2113/99.6.1145.

Owen, N.D., Ciobanu, C.L., Cook, N.J., Slattery, A., Basak, A., 2018. Nanoscale study of clausthalite-bearing symplectites in Cu-Au-(U) ores: implications for ore genesis. Minerals 8, 67. https://doi.org/10.3390/min8020067.

Palarea-Albaladejo, J., Martín-Fernández, J.A., 2013. Values below detection limit in compositional chemical data. Anal. Chim. Acta 764, 32–43. https://doi.org/10.1016/j.aca.2012.12.029.

Palarea-Albaladejo, J., Martín-Fernández, J.A., 2015. zCompositions—R package for multivariate imputation of left-censored data under a compositional approach. Chemometr. Intell. Lab. Syst. 143, 85–96. https://doi.org/10.1016/j.chemolab.2015.02.019.

Pearson, K., 1897. Mathematical contributions to the theory of evolution: on a form of spurious correlation which may arise when indices are used in the measurements of organs. Proc. R. Soc. London 60, 489–498. https://doi.org/10.1098/rspl.1896.0076.

Putnis, A., 2002. Mineral replacement reactions: from macroscopic observations to microscopic mechanisms. Mineral. Mag. 66, 689–708. https://doi.org/10.1180/0026461026650056.

Reeve, J.S., Cross, K.C., Smith, R.N., Oreskes, N., 1990. Olympic Dam copper-uranium-gold-silver deposit. In: Hughes, F.E. (Eds.), Geology of the Mineral Deposits of Australia and Papua New Guinea: Austral. Inst. Min. Metal., Monograph 14, p. 1009–1035.

Richards, J.P., Mumin, A.H., 2013. Magmatic-hydrothermal processes within an evolving

Earth: Iron oxide-copper-gold and porphyry Cu ± Mo ± Au deposits. Geology 41, 767–770. https://doi.org/10.1130/G34275.1.

Richards, J.P., López, G.P., Zhu, J.J., Creaser, R.A., Locock, A.J., Mumin, A.H., 2017. Contrasting tectonic settings and sulfur contents of magmas associated with cretaceous porphyry Cu ± Mo ± Au and intrusion-related iron oxide Cu-Au deposits in Northern Chile. Econ. Geol. 112, 295–318. https://doi.org/10.2113/econgeo.112.2.295.

Rollog, M., Cook, N.J., Guagliardo, P., Ehrig, K.J., Kilburn, M., 2019. In situ spatial distribution mapping of radionuclides in minerals by nanoSIMS. Geochem. Explor. Environm. Anal. https://doi.org/10.1144/geochem2018-038. (in press).

Schmandt, D.S., Cook, N.J., Ciobanu, C.L., Ehrig, K.J., Wade, B.P., Gilbert, S., Kamenetsky, V.S., 2017. Rare earth element fluorocarbonate minerals from the Olympic Dam Cu-U-Au-Ag deposit, South Australia. Minerals 7, 202. https://doi.org/10.3390/min7100202.

Skirrow, R.G., Bastrakov, E.N., Barovich, K., Fraser, G.L., Creaser, R.A., Fanning, C.M., Raymond, O.L., Davidson, G.J., 2007. Timing of iron oxide Cu-Au-(U) hydrothermal activity and Nd isotope constraints on metal sources in the Gawler craton, South Australia. Econ. Geol. 102, 1441–1470. https://doi.org/10.2113/gsecongeo.102.8.1441.

van den Boogaart, K.G., Tolosana-Delgado, R., 2013. In: Analyzing Compositional Data with R. Springer, pp. 258 https://doi.org/10.1007/978-3-642-36809-7.

van den Boogaart, K.G., Tolosana-Delgado, R., Bren, M., 2014. Compositions: Compositional Data Analysis. R package version 1.40-1. https://doi.org/10.1016/j.cageo.2006.11.017.

Verdugo-Ihl, M.R., Ciobanu, C.L., Cook, N.J., Ehrig, K., Courtney-Davies, L., Gilbert, S., 2017. Textures and U-W-Sn-Mo signatures in hematite from the Cu-U-Au-Ag orebody at Olympic Dam, South Australia: defining the archetype for IOCG deposits. Ore Geol. Rev. 91, 173–195. https://doi.org/10.1016/j.oregeorev.2017.10.007.